PHYSICAL REVIEW FLUIDS **4**, 014101 (2019)

Stall of airfoils with blunt noses at low to moderately high Reynolds numbers

Matthew G. Kraljic and Zvi Rusak
Department of Mechanical, Aerospace, and Nuclear Engineering, Rensselaer Polytechnic Institute,
Troy, New York 12180-3590, USA

(Received 13 March 2018; published 10 January 2019)

The onset of leading-edge stall on stationary, smooth, thin, two-dimensional airfoils with various blunt nose shapes of the form $y = \pm k(ax)^{\frac{1}{a}}$ (where $a \geqslant 2$ and k is a constant) at moderately high chord Reynolds numbers (Re) is studied. A reduced-order, multiple-scale model problem is developed and is complimented by direct numerical simulations for low Re and numerical computations using a Reynolds-averaged Navier-Stokes (RANS) flow solver for moderately high Re. The asymptotic theory results in a description of the flow around a thin airfoil composed of an outer region about a majority of the airfoil's chord, and an inner region, surrounding the nose, that match each other. The classical thin airfoil theory dominates the outer region. The coordinates in the inner region are scaled with respect to a characteristic length of the nose and the Reynolds number is modified (Re_M) in order to account for the acute velocity changes in the inner region, where both near-stagnation and high-suction areas appear. The far field of the inner region is described by a symmetric effect due to nose shape and an asymmetric effect with a lumped circulation parameter ($\tilde{A}$) due to angle of attack and camber. The inner flow problem is solved numerically using a transformation from the physical domain to a computational domain and a second-order finite-difference scheme for integrating the vorticity and stream function. The computed results demonstrate numerical convergence with mesh refinement. The inner region solutions reveal, for various values of a, the nature of the flow around the nose and the inception of global separation and stall as $\tilde{A}$ increases above a certain critical value, $\tilde{A}_s$, at fixed a and Re_M. For $a \geqslant 2$, the value of $\tilde{A}_s$ decreases with Re_M up to a limit value, $\mathrm{Re}_{M,\mathrm{lim}}$, above which unsteady effects increase $\tilde{A}_s$ and delay the onset of stall. For airfoils with the same thickness ratio and position of maximum thickness, global stall is delayed to higher angles of attack as a is increased above 2. The results of the RANS computations for various a show matching with the asymptotic results in a certain region of Re_M values, as well as extend the stall predictions of $\tilde{A}_s$ to higher Re_M. Parametric studies provide data for the design of novel airfoils with blunt noses and higher stall angles of attack at various Re.

DOI: 10.1103/PhysRevFluids.4.014101

I. INTRODUCTION

The stall of airfoils is a fundamental physical phenomenon in fluid mechanics and aerodynamics which refers to the sudden separation of flow from the surface of the airfoil, resulting in a precipitous loss of lift, increase of drag, and change of pitching moment when the oncoming flow angle of attack is above a certain critical value. Stall may have both detrimental and beneficial effects on various engineering flow systems. It presents a significant limitation to the design of aircraft wings and stabilizers, propeller and rotorcraft blades, jet-engine compressors and turbine blades, and submarine fins and control surfaces. On the other hand, stall is useful for decelerating systems (spoilers) of aircraft and high-speed cars and for limiting the speed of rotating wind turbine blades

2469-990X/2019/4(1)/014101(34)

in order to prevent overpower situations and catastrophic failures. Stall also appears in the flight of birds and insects (landing and hovering) as well as in marine life motion.

The classical experimental investigations of Jones [1], Jacobs and Sherman [2], Abbott and von Doenhoff [3], and Tani [4] and the modern works by Selig *et al.* [5] and Yen and Huang [6] provide the stall angle of attack for various thin airfoil shapes with small camber and parabolic noses. The experiments demonstrate that the stall angle is a function of chord Reynolds number (Re) and airfoil geometry. Stall angle increases with Re for $\mathrm{Re} > 100\,000$ as well as with the increase of the thickness ratio, δ, or the nose radius of curvature, R_n.

Two types of stall phenomena are known to occur on stationary airfoils. *Leading-edge stall* occurs on airfoils that are relatively thin, having thickness ratios of no more than 14%, typical of wing sections of common aircraft that operate at both low and high subsonic speeds. In this case, the separation zone is generated very close to the leading edge of the airfoil and grows as the angle of attack of the airfoil is increased. The loss of lift resulting from this stall phenomenon is rapid and abrupt. On the other hand, *trailing-edge stall* is predominant on airfoils with thickness ratios greater than 15%, typical of training and heavy low-speed aircraft. Here, the separation zone builds up from the trailing edge of the airfoil and moves upstream toward the nose as the angle of attack is increased. The loss of lift resulting from this type of stall is gradual with the increase of angle of attack. In the present study, we focus solely on the mechanism of the onset of the leading-edge stall on a stationary airfoil in a uniform and incompressible steady flow with no background turbulence.

The leading-edge stall of airfoils is preceded by the appearance of a recirculation bubble located in the boundary layer. This bubble is formed at an angle of attack which is lower than the stall angle of the airfoil. The Pavelka and Tatum [7] experiments demonstrate the existence of this prestall separation bubble. For $\mathrm{Re} < 20\,000$, the flow all around the airfoil is laminar and the short bubble grows in size as the angle of attack is increased. At a certain angle of attack, the bubble bursts, resulting in a long laminar separation zone which defines the stall of the airfoil (with transition to turbulence far downstream). When $30\,000 < \mathrm{Re} < 300\,000$, the appearance of the laminar separation bubble is accompanied by a transition to turbulence above the airfoil at prestall states. The stall of the airfoil still results from the bursting of the separation bubble. For higher Reynolds numbers, $\mathrm{Re} > 500\,000$, the short bubble induces immediate transition to a turbulent boundary layer. The turbulent boundary layer is able to delay the effect of the adverse pressure gradient by keeping the bubble size small (less than 1% of the airfoil's chord). As the angle of attack is increased, the bubble size decreases, the adverse pressure gradient becomes more severe, and the turbulent boundary layer eventually separates from the surface of the airfoil, which results in stall.

To the best of our knowledge, there are no experimental studies of the stall of airfoils with blunter noses than that of the classical airfoils with a parabolic nose.

In addition to the experimental work on the subject of stall, a number of theoretical studies have been performed with the goal of predicting the stall angle of attack of airfoils. Werle and Davis [8] solved the laminar boundary-layer parabolic differential equations for an incompressible flow past a canonic parabola. Their approach, however, resulted in a Goldstein-type singularity as the separation point is approached due to a lack of complete interaction between the separation zone and the outer flow region. In an effort to rectify this singularity, Stewartson [9] and, independently, Ruban [10] used a marginal separation theory (MST), triple-deck method, to allow for a more complete interaction between the various flow regions. This theory uses three regions (decks) corresponding to different regions of the flow. The upper deck corresponds to the outer inviscid flow region. The lower deck is within the boundary layer and surrounds the separation point. The lower and upper decks are permitted to interact with each other through an intermediate region known as the middle deck. Their results demonstrate a trend of angle of attack of stall inception which decreases with the increase of Re. This is opposite the trend found by the experimental studies described above. This trend is a result of the various regions of the triple-deck approach being scaled with inverse powers of Reynolds number. Such a scaling reduces the size of the lower deck to a point in the limit as Re approaches infinity. As the lower deck shrinks in size, the short recirculation bubble, which is present at prestall states, begins to dominate the lower deck. The MST is unable to observe the stall-delaying behavior of the turbulent boundary layer resulting from this short recirculation bubble. Therefore, the MST is limited to the prediction of the appearance of the short recirculation bubble in a prestall state of marginal separation.

In a set of two recent papers, Rusak and Morris [11] and Morris and Rusak [12] studied the leading-edge stall of thin airfoils with a parabolic nose at subsonic speeds and at low to moderately high Reynolds numbers. They accounted for the complete interactions between the near-wall viscous boundary-layer flow and the outer inviscid flow. The asymptotic analysis for thin airfoils resulted in a simplified model problem of a uniform, steady stream at a rescaled Reynolds number, Re_M, past a semi-infinite, stationary, canonic parabola with a far-field circulation governed by a parameter $\tilde{A}$. This parameter is related to the angle of attack, nose radius of curvature, and camber of the airfoil and to the flow Mach number. It results from the asymptotic matching between the outer flow around most of the airfoil chord (that is described by Prandtl's thin airfoil theory including the Kutta condition at the trailing edge) and the inner viscous flow around the parabolic nose. The model parabola problem was solved using numerical simulations based on the Navier-Stokes equations for low Re_M, $100 < \mathrm{Re}_M < 2\,000$, and using the Reynolds-averaged Navier-Stokes (RANS) formulation for high Re_M, $1\,000 < \mathrm{Re}_M < 100\,000$. The computed results were used to determine the special value of $\tilde{A}_s$ where a large separation zone first appears in the nose flow, concurrent with a sudden drop of the maximum suction. The variation of $\tilde{A}_s$ with Re_M was presented as a universal parameter for stall prediction. The predicted $\tilde{A}_s$ values showed two significant results: (1) decrease with Re_M and agreement with the predictions according to the MST theory [13] for $100 < \mathrm{Re}_M < 300$ and (2) increase with Re_M in the range $300 < \mathrm{Re}_M < 2\,000$ and matching with the RANS predictions in the range $1\,000 < \mathrm{Re}_M < 2\,000$. In this range of Re_M, convective waves are shed out of the local separation zone and help to delay the onset of global separation and stall to values of $\tilde{A}_s$ above those predicted by MST. These waves appear for the first time at values of $\tilde{A}$ slightly above the MST prediction. Moreover, the RANS predictions for high-Re flows show that the further increase of $\tilde{A}_s$ with Re_M above the MST predictions is caused by the turbulent flow behind the localized separation zone. These values of $\tilde{A}_s$ were used for the prediction of the stall angle α_s as a function of Re of various airfoil geometries and were compared with stall results from much of the available experimental data at chord Reynolds numbers $\mathrm{Re} > 40\,000$ (see details in Ref. [11]). The theoretical predictions of the stall angle of attack are within 1.5 deg above the experimental values (less than 10% error).

To the best of our knowledge, the stall of airfoils with noses blunter than the classical parabolic nose shapes was never studied either theoretically or numerically (as well as not experimentally). It should be mentioned, however, that the designs proposed by Liebeck [14] suggest a class of airfoils for generating high lift in incompressible flows. These designs indicate that making the parabolic nose more blunt results in the increase of the angle of attack of stall. This trend is also supported by the theory in Refs. [11,12], which showed that the stall angle is proportional to $\sqrt{R_n}$ and for classical parabolic nose airfoils increases with the increase of the nose radius of curvature or airfoil's thickness ratio. However, for parabolic nose airfoils, once thickness ratio is increased above 14% they are dominated and limited by the trailing-edge stall phenomenon, which reduces the angle of stall. Our idea is that the nose curvature is increased without any increase of thickness ratio above 12%, such that leading-edge stall is delayed and trailing-edge stall does not dominate and limit the aerodynamics of novel airfoils. This also allows the increase of airfoil volume without increase in thickness ratio to contain more fuel inside the wings.

The present study focuses on the prediction of the onset of leading-edge stall of thin airfoils with noses that are blunter than parabolic shapes. The nose shape is described by $y = \pm k(ax)^{\frac{1}{a}}$ (where $a \geqslant 2$). Thereby, the radius of curvature at the leading edge turns from finite when $a = 2$ to infinite when $a > 2$ and this allows more flow symmetry around the nose with increase of a above 2 and may help delay stall. Such a theoretical study has never been conducted. The extension of the results of Morris and Rusak [12] to such airfoils is not trivial since the nose shape parameter, a, complicates the mathematical analysis of the problem and results in a more detailed physics, specifically as a is increased above 2. For example, the blunter nose shapes have an infinite curvature at the leading edge and as a result there is no natural length scale of the nose as there was for the parabolic nose with $a = 2$ where the nose radius of curvature dominates the problem. We first determined through the analysis the length scale, R_n, that characterizes nose shapes with $a > 2$ and matches the case of $a = 2$ as well. Using that length scale, we developed asymptotic approximations of the flow in inner and outer regions around the airfoil. In the inner region, Re_M is based on this definition of R_n. Moreover, the matching of flow behavior between these regions in an intermediate region is more complicated than that for the case $a = 2$ since it requires a careful, more general, expansion of the flow behavior when the distance from the outer region toward the leading edge is reduced and when the distance from the leading edge is increased. Such a detailed analysis has never been performed. The resulting flow problem in the inner region involves many terms that do not exist when $a = 2$. Thereby, it also complicates the numerical solution of this problem and requires the development of a new general finite-difference code that can handle any value of a, not only $a = 2$, as was done by Morris and Rusak [12]. The computed results of the stall parameter, $\tilde{A}_s(\mathrm{Re}_M; a)$, provide insight into the possible delay of stall using nose shapes with $a > 2$. Moreover, the present analysis shows that design of thin airfoils with blunter nose shapes than parabolic is definitely feasible and can impact the angle-of-attack envelope of operation of wings of low-speed as well as high-speed aircraft and rotor blades of helicopters and turbines.

The present results are limited to the appearance of only leading-edge stall on thin airfoils with thickness ratios less than or equal to 12%, camber ratio up to 4%, and angles of attack up to 14 deg. At higher thickness ratios or camber ratios, trailing-edge stall may dominate the flow and is not modeled by the present study. Also, present computations are limited to flow Reynolds numbers Re based on airfoil's chord up to 300 000 where the boundary layer flow is mostly laminar and there is no imposed transition to turbulence by tripping the boundary layer. There is no perturbation or turbulence in the upstream flow. When upstream turbulence exists or when transition is imposed by tripping, they may also effect the appearance of stall to higher angles of attack; see, for example, the recent simulations of Balakumar [15]. This observation agrees with Morris and Rusak's [12] theory; they showed that the appearance of unsteady shedding of vortices from the leading-edge separation zone when $\mathrm{Re}_M > 300$ (or $\mathrm{Re} > 20\,000$) is the mechanism of increase of stall angle of attack in classical airfoils. With the increase of Re above 300 000, these shedding waves become more turbulent and help to further delay the stall angle of attack. Tripping of the boundary layer, specifically between the maximum suction point and the nose of the separation bubble, helps to ignite this mechanism.

We note that within these limitations, the results in Refs. [11,12] show that the prediction of the stall angle of attack is accurate within less than 1.5 deg with respect to experimental data for many practical thin airfoil shapes and correctly predicts the change of their stall angle of attack with Reynolds number, airfoil thickness, or nose radius of curvature. This wide range of agreement supports the approach of the present paper.

The outline of the paper is as follows. The mathematical model and the reduced order model for leading-edge stall analysis are formulated in Sec. II. Section III describes the numerical approach to solving the inner flow problem. Mesh convergence studies are presented in Sec. IV. The results of the numerical simulation for the inner nose problem are presented in Sec. V. The results of the inner flow problem are extended to higher Reynolds numbers using a Reynolds-averaged-Navier-Stokes method, presented in Sec. VI. A summary of results and conclusions is given in Sec. VII.

II. MATHEMATICAL MODEL

We consider a smooth, thin airfoil with a shape given by $y = \delta c F_{u,l}(x/c)$ for $0 \leqslant x \leqslant c$ and $0 < \delta \ll 1$, where c is the chord, δ is the thickness ratio, and $F_{u,l}(x/c)$ are the shape functions of the upper and lower surfaces of the airfoil, respectively. The x axis goes along the free stream direction, with a unit vector $\mathbf{i}$, and measures distance from the leading edge, where $x = 0$. The

y axis, with a unit vector $\mathbf{j}$, measures distance normal to the x axis. The airfoil is assumed to be at a low angle of attack, α (in radians), with respect to the free stream direction, such that the scaled angle of attack in terms of the thickness ratio, $A = \alpha/\delta$, is $O(1)$. The airfoil shape function is given by $F_{u,l}(x/c) = C_a(x/c) \pm t(x/c) - Ax/c$. Here, the camber function is $C_a(x/c)$ and the thickness function is $t(x/c)$, where at the trailing edge $C_a(1) = t(1) = 0$. These functions are defined by $C_a(x/c) = m_1(x/c) + m_2(x/c)^2 + \cdots$ and $t(x/c) = h_0(x/c)^{\frac{1}{a}} + h_1(x/c) + h_2(x/c)^2 + \cdots$, where $m_1, m_2, \ldots, h_0, h_1, h_2, \ldots$ are given coefficients and $a \geqslant 2$. The airfoil's nose is characterized by a length scale, $R_n = a^{\frac{-1}{a-1}}(\delta h_0)^{\frac{a}{a-1}}c$, that is much smaller than the chord. Then, near the leading edge, the airfoil exhibits a canonic shape in terms of R_n, $y/R_n = (ax/R_n)^{1/a}$.

We note that the equation for $F_{u,l}(x/c)$ includes a term Ax/c. This term represents the leading order of rotating the base airfoil shape about the leading edge at the origin by the angle of attack α with respect to the uniform flow direction. A similar approach of formulating the airfoil geometry in aerodynamic mathematical analysis was used in the classical book by Cole and Cook [16], p. 47, Eq. (3.1.2). In the case of thin airfoils (with $0 < \delta \leqslant 12\%$) with small camber ratio (less than 4%) at low angles of attack (up to 14 deg) that we study in this paper, this formulation is consistent with all the asymptotic steps of the analysis below and provides sufficiently accurate predictions of airfoils' aerodynamics behavior with a relative error on the order $O(\delta^2, \alpha^2)$.

The fluid is Newtonian and the flow around the airfoil is two dimensional, incompressible (constant density), and viscous with constant free upstream velocity U_∞, pressure P_∞, and density ρ_∞ and with no upstream perturbation or turbulence. The Reynolds number based on chord ($\mathrm{Re} = \rho_\infty U_\infty c/\mu_\infty$) is moderately high with viscosity, μ_∞, given by the free stream temperature, T_∞. We focus on the case where the flow is attached to the airfoil.

The attached flow over the airfoil is described by the nondimensionalized, two-dimensional, unsteady, incompressible, and viscous Navier-Stokes equations,

$$\nabla \cdot \mathbf{V} = 0, \tag{1}$$

$$\frac{\partial \mathbf{V}}{\partial \tau} + \mathbf{V} \cdot \nabla \mathbf{V} = -\nabla P + \frac{1}{\mathrm{Re}} \nabla^2 \mathbf{V}. \tag{2}$$

Here, τ is the nondimensional time scaled by $\frac{c}{U_\infty}$, x and y are nondimensionalized by c, such that $\bar{x} = \frac{x}{c}$ and $\bar{y} = \frac{y}{c}$, $\nabla = \frac{\partial}{\partial \bar{x}}\mathbf{i} + \frac{\partial}{\partial \bar{y}}\mathbf{j}$, $\mathbf{V}$ is the velocity vector non-dimensionalized by U_∞, and P is the pressure, scaled by the upstream dynamic pressure, $\rho_\infty U_\infty^2$.

The governing equations are subjected to certain boundary and far-field conditions. The flow obeys the no-slip and no-penetration conditions on the airfoil surfaces. In addition, far away from the airfoil, perturbations to the uniform upstream properties decay to zero.

Because $0 < \delta \ll 1$ and $\mathrm{Re} \gg 1$, the analysis of the steady and attached flow around the airfoil, according to Eqs. (1) and (2), is amenable to an asymptotic approach. In order to proceed in such a fashion and establish a simplified physical model of the flow around the airfoil, the flow is studied in two regions of different length scales: an inner region around the nose of the airfoil that is characterized by the length scale R_n and an outer region around most of the airfoil away from the nose that is characterized by the length scale c; see Fig. 1. The inner region exhibits large velocity and pressure gradients resulting from the stagnation region near the leading edge, on the lower surface of the nose, and the subsequent acceleration of the flow around the curved nose to a point on the upper surface at which the maximum velocity and minimum pressure are reached. The viscous boundary layer splits at the stagnation point and develops as a thin layer along the nose surfaces. In the inner region, the flow is described by a rescaled version of (1) and (2) with the no-slip and no-penetration conditions on the nose surfaces. On the other hand, the outer region exhibits relatively small velocity and pressure changes from the uniform stream properties. The boundary layers of the outer region continue to develop from the inner region and stay attached and thin all along the upper and lower surfaces. Therefore, the effect of the boundary layer on the outer

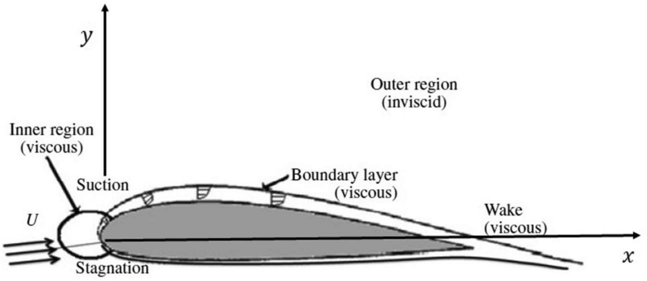

FIG. 1. The physical model and various regions studied.

flow is negligible and the classical, inviscid-flow, thin-airfoil theory of Prandtl may apply in the outer region with acceptable accuracy. The flow behavior in the overlap region between the inner and outer regions must asymptotically match as distance from the leading-edge increases from below R_n to c. Therefore, the far-field behavior of the inner region must match with the near-nose behavior of the outer region. Since the boundary layer in the outer region is thin, the development of the boundary layer does not affect the inner region flow behavior ahead of it (the flow in the boundary layer is parabolic in nature). The inner region boundary layer, on the other hand, is significantly affected by the development of the flow in the outer region near the nose, which dictates the far field of the inner region. By establishing the matching between the flow behavior in the overlap region between the inner and outer regions, the problem is reduced to that of a flow around the canonic nose of the airfoil with a far field given by the inviscid thin airfoil theory. Stall of the airfoil is then determined when the boundary layer suddenly expands and separates from the nose.

A. Outer region

In the outer region, we define coordinates $\bar{x} = \frac{x}{c}$ and $\bar{y} = \frac{y}{c}$. Neglecting the thin boundary layer, the steady and attached flow in the outer region is considered inviscid, irrotational, and potential. Therefore, a velocity potential, $\phi(\bar{x}, \bar{y}; \delta, A)$, can be defined such that the velocity vector is given by $\mathbf{V} = \boldsymbol{\nabla}\phi$. In the inviscid limit of (1) and (2), ϕ obeys

$$\nabla^2\phi = 0, \tag{3}$$

the no-penetration condition, $\frac{\partial\phi}{\partial\bar{n}} = 0$, at every point of the airfoil surfaces (here, $\bar{n}$ is the nondimensional distance along the local, normal unit vector to the airfoil surface), and the decay of ϕ to $\bar{x}$ at distances far from the airfoil.

Following Prandtl's thin-airfoil theory [17], the velocity potential, $\phi(\bar{x}, \bar{y})$, may be given in the limit as $\delta \to 0$ with a fixed A by the asymptotic approximation,

$$\phi(\bar{x}, \bar{y}; \delta, A) = \bar{x} + \delta\phi_1(\bar{x}, \bar{y}; A) + O(\delta^2, \alpha^2). \tag{4}$$

Here, ϕ_1 is the velocity perturbation potential which obeys the Laplace equation,

$$\nabla^2\phi_1 = 0. \tag{5}$$

The no-penetration condition on the airfoil surfaces becomes

$$\frac{\partial\phi_1}{\partial\bar{y}}(\bar{x}, \bar{y} \to 0^{\pm}; A) = \frac{dF_{u,l}(\bar{x})}{d\bar{x}} \quad \text{for } 0 < \bar{x} \leqslant 1. \tag{6}$$

Also, the potential ϕ_1 must decay to zero with distances far from the airfoil surface. As $\bar{y}$ approaches the upper surface, $\bar{y} \to 0^+$, and as $\bar{y}$ approaches the lower surface, $\bar{y} \to 0^-$.

The solution of ϕ_1 is given by [18]

$$\phi_1(\bar{x}, \bar{y}; A) = \phi_{1t}(\bar{x}, \bar{y}) + A\phi_{1\alpha}(\bar{x}, \bar{y}), \tag{7}$$

where

$$\phi_{1t}(\bar{x},\bar{y}) = \frac{1}{\pi c}\int_0^c t'\left(\frac{\xi}{c}\right)\log\sqrt{(\bar{x}-\xi)^2+\bar{y}^2}\,d\xi, \tag{8}$$

$$\phi_{1\alpha}(\bar{x},\bar{y}) = -\frac{1}{\pi c}\int_0^c \omega\left(\frac{\xi}{c}\right)\arctan\left(\frac{\bar{y}}{\bar{x}-\xi}\right)d\xi + \tilde{\Gamma}. \tag{9}$$

Here, t' denotes the derivative of the thickness function with respect to $\frac{\xi}{c}$. Using the coordinate transformation, $\frac{\xi}{c} = \frac{1}{2}[\cos(\vartheta)+1]$, where $0 \leqslant \vartheta \leqslant \pi$, the function ω is given by

$$\omega\left(\frac{\xi}{c}\right) = \omega_0\sqrt{\frac{1-\xi/c}{\xi/c}} - \sum_{i=1}^{\infty}\omega_i\sin(i\vartheta), \tag{10}$$

$$\omega_0 = 1 - \frac{1}{\pi A}\int_0^{\pi} C_a'\left(\frac{\xi}{c}\right)d\vartheta, \quad \omega_i = \frac{2}{\pi A}\int_0^{\pi} C_a'\left(\frac{\xi}{c}\right)\cos(i\vartheta)d\vartheta. \tag{11}$$

Here, C_a' denotes the derivative of the camber function with respect to the variable $\frac{\xi}{c}$. Also, $\tilde{\Gamma} = \frac{1}{c}\int_0^c \omega(\frac{\xi}{c})d\xi$.

Let $\bar{r} = \sqrt{\bar{x}^2+\bar{y}^2}$ and $\theta = \arctan\frac{\bar{y}}{\bar{x}}$, such that $\bar{x} = \bar{r}\cos\theta$ and $\bar{y} = \bar{r}\sin\theta$, where $0 \leqslant \theta \leqslant 2\pi$. As $\bar{y} \to 0^+$, $\theta \to 0$, and as $\bar{y} \to 0^-$, $\theta \to 2\pi$. As the leading edge of the airfoil is approached, $\bar{r} \to 0$, the asymptotic exspansion of ϕ_1, from Eqs. (7)–(9), is given by

$$\phi_1(\bar{x},\bar{y};A) = \frac{h_0}{\cos\psi}\bar{r}^{\frac{1}{a}}\sin\left(\frac{\theta}{a}+\psi\right) + 2A\omega_0\sqrt{\bar{r}}\cos\left(\frac{\theta}{2}\right) + O(\bar{r}). \tag{12}$$

Here, $\psi = \frac{\pi}{2} - \frac{\pi}{a}$. This maintains the symmetry of the first term about the negative $\bar{y}$ direction, for which $\theta = \pi$. Note that the asymptotic expansion in Eq. (12) matches the leading-order term of the no-penetration condition in Eq. (6) as $\bar{x} \to 0^+$, i.e.,

$$\frac{\partial\phi_1}{\partial\bar{y}}(\bar{x},\bar{y}\to 0^{\pm};A) = \pm\frac{h_0}{a}\bar{x}^{\frac{1}{a}-1} + O(1). \tag{13}$$

The first derivative of the first term of Eq. (12) with respect to $\bar{y}$ matches with the right-hand side of Eq. (13), while the first derivative of the second term in Eq. (12) is zero as $\theta \to 0$ or $\theta \to 2\pi$.

From Eqs. (4) and (12), the velocity potential, ϕ, in the limit $\delta \to 0$ with a fixed A, is described by the following asymptotic expansion as $\bar{r} \to 0$:

$$\phi = \bar{x} + \delta\left[\frac{h_0}{\cos\psi}\bar{r}^{\frac{1}{a}}\sin\left(\frac{\theta}{a}+\psi\right) + 2A\omega_0\sqrt{\bar{r}}\cos\left(\frac{\theta}{2}\right) + O(\bar{r})\right] + O(\delta^2,\alpha^2). \tag{14}$$

Equation (14) shows that the structure of the flow in the outer region near the nose of the airfoil maybe described, in the leading order, by a linear combination of a uniform flow, a symmetric flow expansion due to the nose shape, and an asymmetric flow which runs around the nose due to the airfoil's angle of attack and the integrated effect of the camber. Since $\delta h_0 = a^{\frac{1}{a}}(\frac{R_n}{c})^{\frac{a-1}{a}}$ and $A = \frac{\alpha}{\delta}$, Eq. (14) can be rewritten as

$$\phi = \bar{x} + \left[\frac{1}{\cos\psi}\left(\frac{R_n}{c}\right)^{\frac{a-1}{a}}(a\bar{r})^{\frac{1}{a}}\sin\left(\frac{\theta}{a}+\psi\right) + \sqrt{2}\alpha\omega_0\sqrt{2\bar{r}}\cos\left(\frac{\theta}{2}\right) + O(\bar{r})\right] + O(\delta^2,\alpha^2). \tag{15}$$

Equation (15) shows that the velocity $\mathbf{V}$ as well as the pressure P change like $\bar{r}^{\frac{1}{a}-1}$ and become singular as $\bar{r} \to 0$, independent of θ. This is an expected leading-edge singularity since the thin-airfoil theory assumes small disturbances form a uniform flow while, at the nose region, there are significant velocity changes from a uniform flow. The singular behavior becomes dominant when

$0 < \bar{r} < \frac{R_n}{c}$. This singularity suggests that the flow near the nose must be analyzed in an inner region around the nose with scaled coordinates based on R_n.

B. Inner region

In the inner region, around the nose of the airfoil, the characteristic length is R_n. We define rescaled coordinates $x^* = \frac{x}{R_n}$, $y^* = \frac{y}{R_n}$. Time is rescaled as $\tau^* = \frac{tR_n}{U_\infty}$. The use of rescaled coordinates magnifies the view of the flow around the nose to be able to accurately capture the significant changes of the velocity from stagnation on the lower surface to high suction on the upper surface that occur in a small region of size R_n around the leading edge. It also avoids the need to apply adaptive mesh techniques to accurately resolve the flow structure around the airfoil's nose (Webster *et al.* [19]).

Then, Eqs. (1) and (2) become

$$\nabla^* \cdot \mathbf{V}^* = 0, \tag{16}$$

$$\frac{\partial \mathbf{V}^*}{\partial \tau^*} + \mathbf{V}^* \cdot \nabla^* \mathbf{V}^* = -\nabla^* P^* + \frac{1}{\mathrm{Re}_M} \nabla^{*2} \mathbf{V}^*. \tag{17}$$

Here, V^* and P^* are the nondimensional velocity vector and pressure in the inner region, scaled by U_∞ and ρU_∞^2, respectively. The modified Reynolds number of the inner region is based on R_n,

$$\mathrm{Re}_M = \mathrm{Re}\frac{R_n}{c}, \tag{18}$$

and $\nabla^* = \frac{\partial}{\partial x^*}\mathbf{i} + \frac{\partial}{\partial y^*}\mathbf{j}$. Also, as $\delta \to 0$ with a fixed A, the airfoil nose becomes, at leading order, $y^* = \pm k(ax^*)^{\frac{1}{a}}$ for $x^* \geqslant 0$. For all time, t^*, the flow obeys the no-penetration and no-slip conditions along the inner nose surface.

Let $r^* = \sqrt{x^{*2} + y^{*2}}$ and $\theta^* = \arctan \frac{y^*}{x^*}$, such that, $x^* = r^* \cos\theta^*$ and $y^* = r^* \sin\theta^*$.

As the far field of the inner region is approached, $r^* \gg 1$, the flow is steady and nearly inviscid, except for the thin boundary layer attached to the nose surface. Then, a nondimensional velocity potential, $\phi^*(x^*, y^*; A)$ scaled by $U_\infty R_n$, exists in the far field of the inner region, where $\mathbf{V}^* = \nabla^*\phi^*$. The velocity potential obeys the Laplace equation, $\nabla^{*2}\phi^* = 0$. In the limit $\delta \to 0$, the potential ϕ^* is approximated, when $r^* \gg 1$, by the following asymptotic expansion of certain fundamental solutions of the Laplace equation that are chosen to later match with the outer solution:

$$\phi^*(x^*, y^*; \tilde{A}) = x^* + \tilde{A}\sqrt{2r^*}\cos\left(\frac{\theta^*}{2}\right) + k_1(ar^*)^{\frac{1}{a}} \sin\left(\frac{\theta^*}{a} + \psi\right) + O(r^{*\gamma}). \tag{19}$$

Here, $0 < \gamma < \frac{1}{a}$. The constant coefficient k_1 and the circulation parameter, $\tilde{A}$, are determined by the matching between the inner and outer approximations of the velocity potential. The solution given by Eq. (19) may contain additional fundamental solutions of the Laplace equation of the shape $r^{*m}\cos(m\theta^*)$ or $r^{*m}\sin(m\theta^*)$, where $0 < m < 1/a$, the coefficients of which are zero when matched with the near nose solution of the outer region.

C. Matching between inner and outer expansions

Let $r = \sqrt{x^2 + y^2}$. Then, in the outer region, $r = c\bar{r}$, and in the inner region, $r = R_n r^*$. Also note that $\theta = \theta^*$. The matching of the near-nose outer and far-field inner asymptotic expansions according to Eqs. (14) and (19) is carried out with the help of an intermediate region $\eta(\delta)$, where $r_\eta = \frac{r}{\eta}$ is held fixed in the limit $\delta \to 0$ with a fixed A and

$$0 < \delta^{\frac{a}{a-1}} \ll \eta(\delta) \ll 1 \tag{20}$$

such that, as $\delta \to 0$, $\eta(\delta) \to 0$ and the ratio $\frac{\eta(\delta)}{\delta^{\frac{a}{a-1}}} \to \infty$. The scale $\eta(\delta)$ represents a whole order class of limit between the inner and outer regions and is called the overlap region. Then, as $\delta \to 0$, in the near-nose outer region $\bar{r} = \eta(\delta)\frac{r_\eta}{c} \to 0$ and in the far field of the inner region, $r^* = \eta\frac{r_\eta}{R_n} \to \infty$ (since $R_n \sim \delta^{\frac{a}{a-1}}$).

For matching, the expansions of the velocity potential in the physical scale must read the same, to a certain order, when expressed in the r_η coordinate:

Near-nose outer expansion

$$\Phi = U_\infty c\left\{\frac{x}{c} + \delta\left[\frac{h_0}{\cos\psi}\left(\eta\frac{r_\eta}{c}\right)^{\frac{1}{a}}\sin\left(\frac{\theta}{a}+\psi\right) + 2A\omega_0\sqrt{\eta\frac{r_\eta}{c}}\cos\left(\frac{\theta}{2}\right) + O\left(\eta\frac{r_\eta}{c}\right)\right]\right.$$
$$\left. + O(\delta^2, \alpha^2)\right\}$$

$$\Longleftrightarrow \tag{21}$$

Far-field of the inner expansion

$$\Phi = U_\infty R_n\left\{\frac{x}{R_n} + \tilde{A}\sqrt{2\eta\frac{r_\eta}{R_n}}\cos\left(\frac{\theta}{2}\right) + k_1\left(a\eta\frac{r_\eta}{R_n}\right)^{\frac{1}{a}}\sin\left(\frac{\theta}{a}+\psi\right) + O\left[\left(\eta\frac{r_\eta}{R_n}\right)^{\gamma}\right]\right\}.$$

The leading-order terms shown in Eq. (21) with the same powers of r_η match if

$$k_1 = \frac{1}{\cos\psi}, \quad \tilde{A} = \frac{\alpha\omega_0}{\sqrt{\frac{R_n}{2c}}}. \tag{22}$$

Higher order terms on the order of $O(\delta^2, \alpha^2)$, $O(\delta\eta\frac{r_\eta}{c})$, and $O(R_n(\eta\frac{r_\eta}{R_n})^\gamma)$ are not matched.

The matching of a continuous-flow behavior in the intermediate region between the inner and outer regions results in a special relationship between the circulation parameter, $\tilde{A}$, and the rescaled angle of attack, $A = \alpha/\delta$, the camber effect through ω_0, and the nose characteristic length, R_n/c. The circulation parameter $\tilde{A}$ represents the lumped effect of angle of attack, airfoil camber, and geometry on the far-field flow behavior of the nose region as distance from the leading edge is increased toward the outer region.

The above matching formulates a well-defined, canonic, boundary value problem for the solution of the inner flow around the nose. The inner flow is described by Eqs. (16) and (17) with the no-slip and no-penetration conditions, $\mathbf{V}^* = 0$, along the canonic nose surface $y^* = \pm k(ax^*)^{\frac{1}{a}}$ and with the far-field condition given by Eq. (19) and coefficients in Eqs. (22).

D. Stall prediction

In the present study, we look to numerically solve the flow in the inner region around the canonic nose surface and determine the value of $\tilde{A}$ as a function of Re_M at which a sudden global eruption of the boundary layer occurs. This value is denoted as $\tilde{A}_s(\mathrm{Re}_M; a)$ and is termed the stall circulation parameter,

$$\tilde{A}_s = \frac{\alpha_s\omega_o}{\sqrt{\frac{R_n}{2c}}}. \tag{23}$$

This special value indicates a sufficient condition for the onset of leading-edge stall on the airfoil, $\tilde{A} > \tilde{A}_s$. Then, using Eq. (11) for ω_0, the predicted stall angle of the airfoil is given by

$$\alpha_s = \tilde{A}_s(\mathrm{Re}_M; a)\sqrt{\frac{R_n}{2c}} + \frac{\delta}{\pi}\int_0^\pi C_a'\left(\frac{\xi}{c}\right)d\vartheta + O\left(\frac{1}{2}A_S^2\delta^2\right). \tag{24}$$

The prediction of the stall angle, α_s, is composed of two effects. The first is related to the nose characteristic length, R_n/c, and the stall circulation parameter, $\tilde{A}_s$, as a function of the modified Reynolds number, Re_M, and the nose shape parameter, a. The second effect is related only to the derivative of the camber function. For typical airfoil shapes with thickness ratio $4\% < \delta < 12\%$ and small camber (of less than 4%), the first effect is dominant in determining the stall angle as a function of Re_M and a. On the other hand, for very thin airfoils with $0\% < \delta < 4\%$, the second effect is dominant and the stall angle for such airfoils is nearly independent of the Re_M and a.

At low Reynolds numbers, $100 \leqslant \mathrm{Re}_M \leqslant 1\,250$, we convert the flow problem of Eqs. (16), (17), (19), and (22) into the stream function vorticity formulation and develop in the next section a numerical code for flow simulations around the canonic nose at various values of a, Re_M, and $\tilde{A}$. From these simulations, we determine the value, $\tilde{A}_s(\mathrm{Re}_M; a)$, at which global flow separation occurs and the peak velocity on the upper surface of the nose suddenly drops with the increase of $\tilde{A}$. From this stall onset value, the angle of attack of stall, α_s, can be predicted according to Eq. (24). Since we find that in all computed cases $\tilde{A}_s(\mathrm{Re}_M; a) > 1$, the present analysis shows that the relative error in predicting α_s according to Eq. (24) is $O(\frac{1}{2}\tilde{A}_s^2\delta^2)$, an error that is typically within 1.5 deg.

III. NUMERICAL SIMULATION OF THE INNER PROBLEM

The formulation of the inner flow problem over a canonic nose shape requires the development of a new computational solver for shapes with nose shape parameters $a > 2$.

A. Transformation to a computational domain

The inner region flow around a canonic nose section is described by the two-dimensional, viscous, incompressible, and unsteady Navier-Stokes equations (16) and (17) written in terms of the inner coordinates, x^*, y^*, τ^*. Let Ψ be defined as the stream function and ω as the vorticity, such that the axial and normal velocity components, u^* and v^*, and the vorticity are given by

$$u^* = \frac{\partial \Psi}{\partial y^*}, \quad v^* = \frac{\partial \Psi}{\partial x^*}, \quad \text{and} \quad \omega = \frac{\partial v^*}{\partial x^*} - \frac{\partial u^*}{\partial y^*}. \tag{25}$$

The continuity equation (1) is automatically satisfied by Eq. (25). Also, this allows the momentum equation (2) to be reduced to two equations for the solution of two dependent variables, the stream function and vorticity,

$$\frac{\partial \omega}{\partial \tau^*} + \frac{\partial \Psi}{\partial y^*}\frac{\partial \omega}{\partial x^*} - \frac{\partial \Psi}{\partial x^*}\frac{\partial \omega}{\partial y^*} = \frac{1}{\mathrm{Re}_M}\left(\frac{\partial^2 \omega}{\partial x^{*2}} + \frac{\partial^2 \omega}{\partial y^{*2}}\right), \tag{26}$$

$$\frac{\partial^2 \Psi}{\partial x^{*2}} + \frac{\partial^2 \Psi}{\partial y^{*2}} = -\omega. \tag{27}$$

Equation (26) describes the transport of vorticity in the domain. Vorticity is convected by the flow and diffused by the viscosity, specifically near the solid surface. Equation (27) is the kinematic relationship between vorticity and the stream function. Solving the above equations for Ψ and ω allows for the direct computation of the velocity components, u^* and v^*. Equations (26) and (27) are subjected to both the no-penetration and no-slip conditions, $u^* = v^* = 0$, on the surface of the canonic nose section as well as the far-field condition given by Eq. (19) and coefficients in Eq. (22).

The flow field in the (x^*, y^*) domain is transformed to a Cartesian computational space with the aid of the specially designed transformed coordinates

$$x^* = \frac{\mu^a - \eta^a}{a}, \quad y^* = \mu\eta. \tag{28}$$

In the computational space, η is the coordinate which is normal to the canonic nose surface and μ is the coordinate parallel to the surface. The surface of the canonic nose, $y^* = \pm(ax^* + 1)^{\frac{1}{a}}$, is described by the surface $\eta = 1$ and the flow evolves in the domain given by $-\infty < \mu < \infty$, $\eta > 1$.

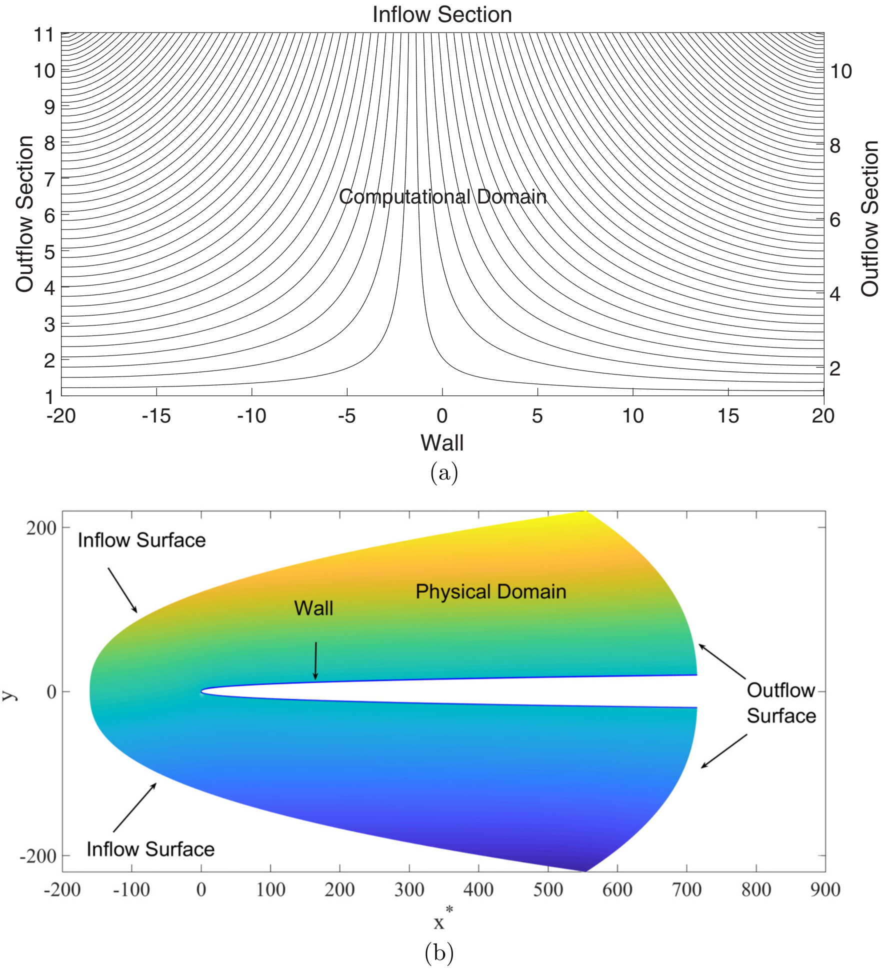

(a)

(b)

FIG. 2. (a) Computational domain with Ψ contours and (b) physical domain for the case of $a = 2$ at $\mathrm{Re}_M = 100$ and $\tilde{A} = 1.5$. The bottom of panel (a), the μ axis, represents the upper (positive) and lower (negative) surfaces of the canonic nose. The top of panel (a) represents the far field away from the nose toward infinity. The left and right sides of panel (a), the η axis, represent the far field away from the nose. The boundaries of panel (b) are the nose wall and the inflow and outflow surfaces.

For the computational implementation, we used a truncated large domain where $-\mu_{\max} \leqslant \mu \leqslant \mu_{\max},\ 1 \leqslant \eta \leqslant \eta_{\max}$. See Fig. 2 for an example of the computational domain and corresponding physical domain and their nose wall at $\eta = 1$, upstream far field at $\eta_{\max} = 11$, and far-field upper and lower outlet boundaries at $\mu = \pm 20$. The case shown is for $a = 2$ at $\mathrm{Re}_M = 100$ and $\tilde{A} = 1.5$. In Fig. 2(a), there are 50 equispaced ψ contours and there is a local separation zone on the positive μ axis at $\mu \sim 3$, which corresponds to a location in the physical domain of $x^* \sim 4,\ y^* \sim 3$. This local separation zone is barley seen in the global, physical scale.

Using the transformed coordinates in Eq. (28), the velocity components are given by

$$V_\mu = \frac{1}{\sqrt{\mu^{2(a-1)} + \eta^2}} \frac{\partial \Psi}{\partial \eta}, \quad V_\eta = -\frac{1}{\sqrt{\mu^2 + \eta^{2(a-1)}}} \frac{\partial \Psi}{\partial \mu}. \tag{29}$$

Rewriting Eqs. (26) and (27) in terms of the transformed coordinates gives

$$\begin{aligned}
&\frac{\partial\omega}{\partial\tau^*}+\frac{1}{\mu^a+\eta^a}\left(\frac{\partial\omega}{\partial\mu}\frac{\partial\Psi}{\partial\eta}-\frac{\partial\omega}{\partial\eta}\frac{\partial\Psi}{\partial\mu}\right)\\
&\quad=\frac{1}{\mathrm{Re}_M}\left[\frac{\partial^2\omega}{\partial\mu^2}K+\frac{\partial^2\omega}{\partial\eta^2}L+2\frac{\partial^2\omega}{\partial\mu\partial\eta}M+\frac{\partial\omega}{\partial\mu}N+\frac{\partial\omega}{\partial\eta}P\right],
\end{aligned}\tag{30}$$

$$\frac{\partial^2\Psi}{\partial\mu^2}K+\frac{\partial^2\Psi}{\partial\eta^2}L+2\frac{\partial^2\Psi}{\partial\mu\partial\eta}M+\frac{\partial\Psi}{\partial\mu}N+\frac{\partial\Psi}{\partial\eta}P=-\omega,\tag{31}$$

where

$$K=\frac{\mu^2+\eta^{2a-2}}{(\mu^a+\eta^a)^2},\tag{32}$$

$$L=\frac{\eta^2+\mu^{2a-2}}{(\mu^a+\eta^a)^2},\tag{33}$$

$$M=\frac{\mu^{a-1}\eta^{a-1}-\mu\eta}{(\mu^a+\eta^a)^2},\tag{34}$$

$$N=\eta^a\mu(1+a)+(1-a)\mu^{a+1}-(1+a)\mu^{a-1}\eta^{2a-2}-(1-a)\eta^{a-2}\mu^{2a-1},\tag{35}$$

$$P=(a+1)\mu^a\eta+(1-a)\eta^{a+1}-(a+1)\mu^{2a-2}\eta^{a-1}-(1-a)\mu^{a-2}\eta^{2a-1}.\tag{36}$$

Note that for the case of $a=2$, $K=L=\frac{1}{\mu^2+\eta^2}$ and $M=N=P=0$. However, when $a>2$, these terms are more complicated and effect the solution of Eqs. (30) and (31).

Since from the definitions of velocity components given in Eq. (29),

$$\frac{\partial}{\partial\mu}[\sqrt{\mu^{2(a-1)}+\eta^2}V_\mu]+\frac{\partial}{\partial\eta}[\sqrt{\mu^2+\eta^{2(a-1)}}V_\eta]=0,\tag{37}$$

in a conservative form, Eq. (30) is given by

$$\begin{aligned}
&\frac{\partial\omega}{\partial\tau^*}+\frac{1}{\mu^a+\eta^a}\left[\frac{\partial}{\partial\mu}(\sqrt{\mu^{2(a-1)}+\eta^2}V_\mu\omega)+\frac{\partial}{\partial\eta}(\sqrt{\mu^2+\eta^{2(a-1)}}V_\eta\omega)\right]\\
&\quad=\frac{1}{\mathrm{Re}_M}\left[\frac{\partial^2\omega}{\partial\mu^2}K+\frac{\partial^2\omega}{\partial\eta^2}L+2\frac{\partial^2\omega}{\partial\mu\partial\eta}M+\frac{\partial\omega}{\partial\mu}N+\frac{\partial\omega}{\partial\eta}P\right].
\end{aligned}\tag{38}$$

Equations (38) and (31) are subject to the no-penetration and no-slip boundary conditions on the surface of the canonic nose given respectively for all time, $\tau^*>0$, by $V_\eta(\mu,\eta=1,\tau^*)=V_\mu(\mu,\eta=1,\tau^*)=0$. The no-penetration condition is also equivalent to $\Psi(\mu,\eta=1,\tau^*)=0$ for all $\tau^*>0$. In the far-field of the inner region, when $\eta\gg 1$, the approximation given in Eq. (19) is equivalent for all $\tau^*>0$ to

$$\Psi(x^*,y^*,\tau^*;\tilde{A})=y^*+\tilde{A}\sqrt{2r^*}\sin\left(\frac{\theta^*}{2}\right)+k_1(ar^*)^{\frac{1}{a}}\cos\left(\frac{\theta^*}{a}+\psi\right).\tag{39}$$

In Eq. (39), we use $x^*=(\mu^a-\eta^a)/a$ and $y^*=\mu\eta$ to compute $r^*=\sqrt{x^{*2}+y^{*2}}$ and $\theta^*=\arctan\frac{y^*}{x^*}$ in terms of μ and η. Along the inlet and outlet far-field sections of the inner region, when $|\mu|\gg 1$, a passive condition $\frac{\partial\Psi^*}{\partial\mu}=0$ is applied.

See the Appendix for the numerical scheme for the solution of the inner problem, numerical boundary conditions, and numerical stability criteria.

IV. MESH CONVERGENCE STUDIES

We first conducted mesh convergence studies for the case of $a = 2.5$ [a $(2.5x^*)^{\frac{2}{5}}$ nose] at two representative Reynolds numbers, $\mathrm{Re}_M = 100$ and 900, each at two values of $\tilde{A}$. The first case focuses on flows at $\mathrm{Re}_M = 100$ with $\tilde{A} = 1.75$ and $\tilde{A} = 1.8$; see Fig. 3 (here, $\mu_{\max} = 20$ and $\eta_{\max} = 11$). In both cases, the long-term dynamics describe a laminar-flow global-separation state. This state represents a leading-edge stall of the nose. Results of the V_μ velocity as a function of μ along a grid line, $\eta = 1.1$, adjacent to the nose surface ($\eta = 1$) from computations with three meshes of $2M = 100$ by $N = 100$, $2M = 200$ by $N = 200$, and $2M = 200$ by $N = 400$ were constructed. Both Figs. 3(a) (for $\tilde{A} = 1.75$) and 3(b) (for $\tilde{A} = 1.8$) demonstrate agreement of computed results from the finer two meshes, within a numerical accuracy of $\sim$0.02, all along the μ axis. Specifically, the details of the flow including the stagnation point, both the negative and positive peaks of velocity, and the velocity within the separation zone are nearly the same for both fine meshes.

In addition, Fig. 4 shows the stream function, Ψ, contour lines according to the mesh $2M = 200$ by $N = 200$ (the red contour lines) and according to the mesh $2M = 200$ by $N = 400$ (the black contour lines). The contour lines computed from the two meshes are essentially the same except for minor changes within the separation zone on the upper surface of the nose, near the leading edge. The computations demonstrate that the mesh with $2M = 200$ by $N = 200$ provides sufficiently accurate results of the flow behavior at the assigned operational conditions. This also matches with the results from Morris and Rusak [12] for the case of $a = 2$ (a parabolic nose), who found that the mesh of $2M = 200$ by $N = 200$ provides, for $0 \leqslant \tilde{A} \leqslant 2$, sufficiently accurate results at $\mathrm{Re}_M = 100$. This mesh is used in all further computations with $100 \leqslant \mathrm{Re}_M \leqslant 400$. For higher values of Re_M, the mesh has to be refined to more accurately capture the details inside the boundary layer.

The second case studies mesh convergence of flows around a nose with $a = 2.5$ at $\mathrm{Re}_M = 900$ with $\tilde{A} = 1$ and $\tilde{A} = 1.5$. For the case of $\tilde{A} = 1$, the laminar flow around the nose is fully attached. Figure 5 describes the computed results of the velocity V_μ along grid lines $\mu = 0.8,\ 1.6,\ 2.4$ from computations with the grids $2M = 100$ by $N = 100$, $2M = 200$ by $N = 200$, and $2M = 200$ by $N = 400$. For all values of μ, agreement of computed results from the two finer meshes (red and black lines) are nearly the same within a numerical accuracy of $\sim$0.01, found by taking the maximum difference between two mesh lines. In addition, Fig. 6 shows the stream function, Ψ, contour lines according to the mesh $2M = 200$ by $N = 200$ (the red contour lines) and according to the mesh $2M = 200$ by $N = 400$ (the black contour lines). The contour lines from the two meshes are essentially the same. The computations demonstrate that the mesh with $2M = 200$ by $N = 400$ provides sufficiently accurate results of the flow behavior at the assigned operational conditions. This mesh is used in all further computations with $400 < \mathrm{Re}_M < 1,250$.

With the increase of $\tilde{A}$ at $\mathrm{Re}_M = 900$, the flow separates and becomes unsteady. For mesh convergence, we focus on the case with $\tilde{A} = 1.5$, where the long-term flow describes a global separation zone on the upper surface of the nose that sheds, from its tail, vortical waves that are convected downstream along the upper surface; see Fig. 7 for the stream function contour lines at $t = 500$. This unsteady flow behavior was studied using three meshes, $2M = 100$ by $N = 100$, $2M = 200$ by $N = 200$, and $2M = 200$ by $N = 400$.

Figure 8 describes the results, computed from the three meshes, of a fast Fourier transform (FFT) analysis of the unsteady V_μ velocity signal at two points, $\mu = 2.6$, $\eta = 1.05$ and $\mu = 6.6$, $\eta = 1.15$, located within the separation zone and behind it, respectively. For both points, the results from the meshes $2M = 200$ by $N = 200$ and $2M = 200$ by $N = 400$ are similar, showing the maximum of the power spectral density (PSD) at a nondimensional frequency (scaled by R_n/U) of about 0.02 at the point $\mu = 2.6$, $\eta = 1.05$ and of about 0.007 at the point $\mu = 2.6$, $\eta = 1.05$. These results demonstrate that the unsteady structures that are shed from the separation bubble are not erratic but are large-scale, coherent structures that are much greater in size than the mesh elements and exhibit a consistent frequency of shedding. The computations also demonstrate that the mesh with $2M = 200$ by $N = 400$ provides sufficiently accurate results of the separated, unsteady flow behavior at the assigned operational conditions.

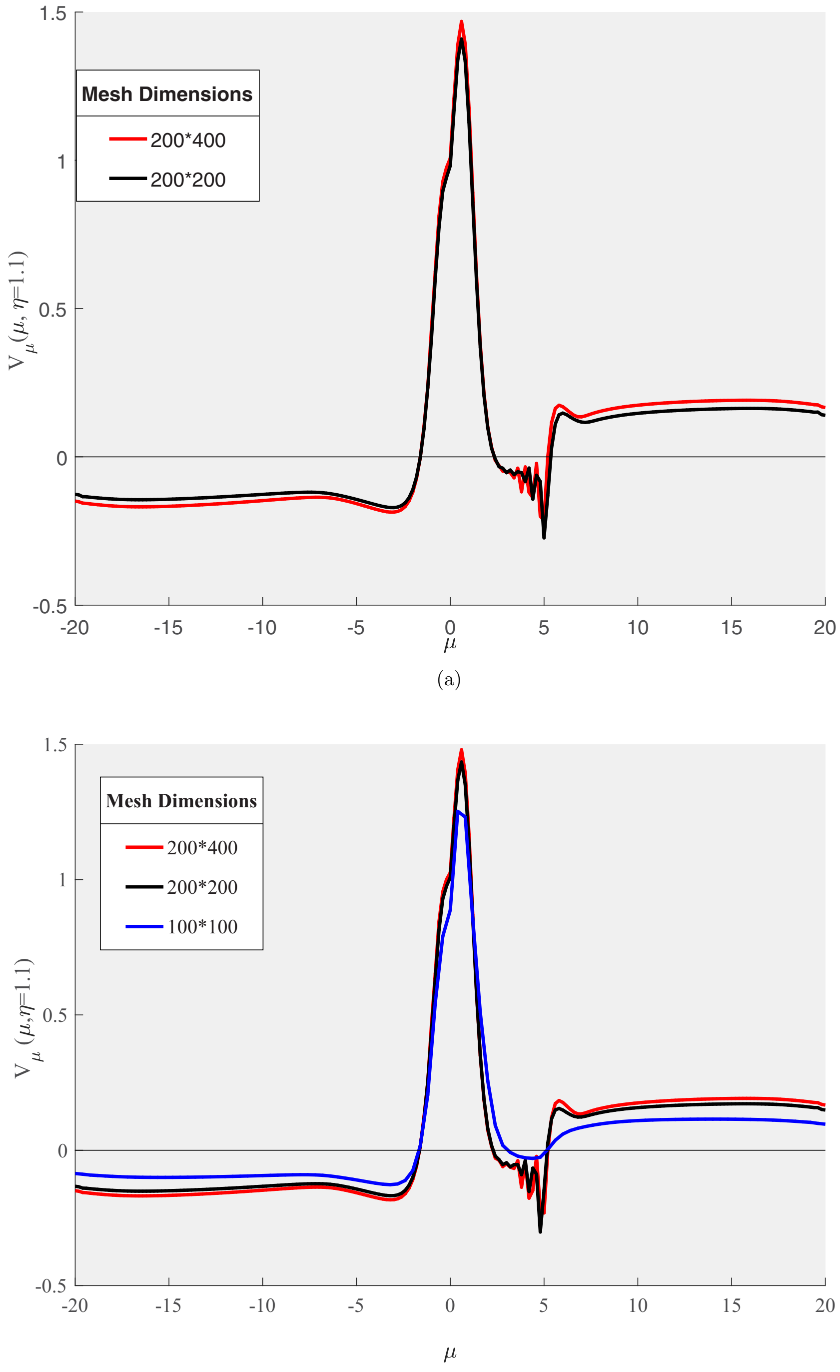

(a)

(b)

FIG. 3. Results of mesh convergence studies for the cases with $a = 2.5$ (a $(2.5x^*)^{\frac{2}{5}}$ nose), $\mathrm{Re}_M = 100$, and (a) $\tilde{A} = 1.75$, (b) $\tilde{A} = 1.8$.

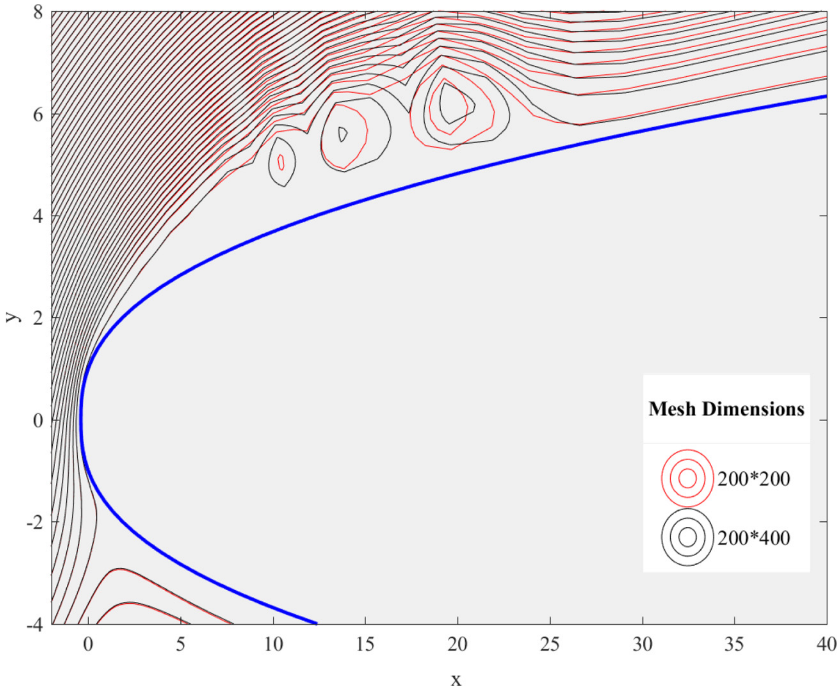

FIG. 4. Comparison of Ψ contour lines for the case with $a = 2.5$ (a $(2.5x^*)^{\frac{2}{5}}$ nose), $\mathrm{Re}_M = 100$, and $\tilde{A} = 1.8$. The red lines are results from the mesh with $2M = 200$ by $N = 200$. The black lines are results from the mesh with $2M = 200$ by $N = 400$.

Results of time-asymptotic states of flows around a parabolic ($a = 2$) nose at various $\tilde{A}$ with $\mathrm{Re}_M = 100$ are shown in Fig. 9. At $\tilde{A} = 0$, the flow expands symmetrically around the nose. The boundary layers develop with distance from the leading edge [Fig. 9(a)]. At $\tilde{A} = 1.3$ and $\tilde{A} = 1.4$, the flow stays attached to the nose surfaces [Figs. 9(b) and 9(c)]. As $\tilde{A}$ is further increased, the flow exhibits a local separation zone when $\tilde{A}$ is between 1.68 and 1.73. When $\tilde{A}$ increases above 1.75, a large and long global separation zone appears on the upper surface of the nose [Fig. 9(d)]. This

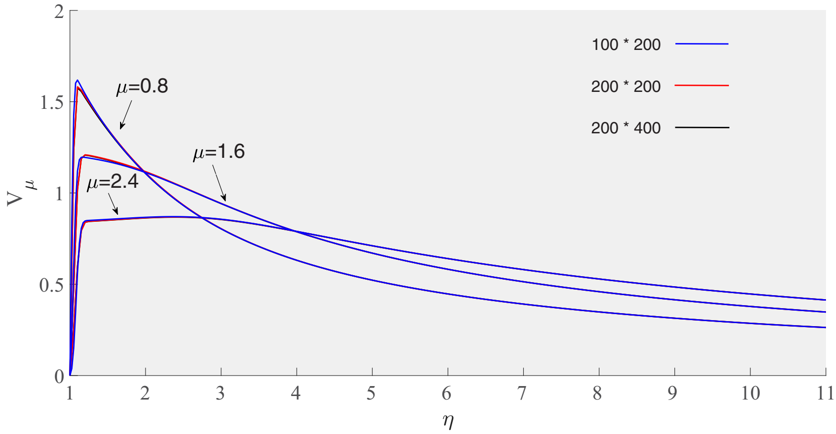

FIG. 5. Results of mesh convergence studies for the cases with $a = 2.5$ (a $(2.5x^*)^{\frac{2}{5}}$ nose), $\mathrm{Re}_M = 900$, and $\tilde{A} = 1$.

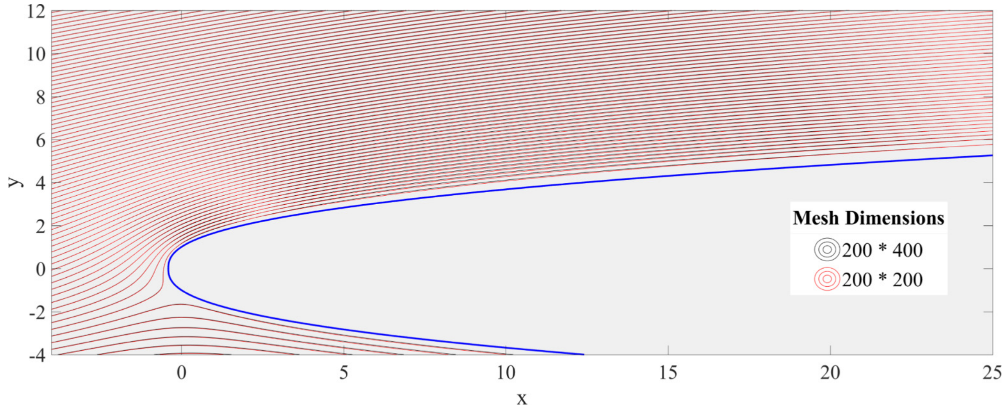

FIG. 6. Comparison of Ψ contour lines for the case with $a = 2.5$ (a $(2.5x^*)^{\frac{2}{5}}$ nose), $\mathrm{Re}_M = 900$, and $\tilde{A} = 1$. The red lines are results from the mesh with $2M = 200$ by $N = 200$. The black lines are results from the mesh with $2M = 200$ by $N = 400$.

indicates the leading-edge stall of an airfoil with a parabolic nose. For $a = 2$ and $\mathrm{Re}_M = 100$, we find that $\tilde{A}_s = 1.75$. This result matches the computations of Morris and Rusak [12] and, therefore, provides a validation of computations with respect to previous studies.

V. COMPUTED RESULTS

We conducted extensive computations of flow behavior in the inner region for various values of the nose shape parameter, a, the modified Reynolds number, Re_M, and the circulation parameter, $\tilde{A}$. The results are presented in the following paragraphs and demonstrate the change of flow structure with the increase of $\tilde{A}$ and a at a fixed value of Re_M. The values of the stall parameter, $\tilde{A}_s$, as a function of Re_M and a at which global separation and stall occur are identified, within numerical accuracy, from these computations.

Computations of time-asymptotic states of flows around a nose with power $a = 2.5$ at $\mathrm{Re}_M = 100$ and various $\tilde{A}$ are shown in Fig. 10. At $\tilde{A} = 1.5$, the flow expands around the nose surfaces and the laminar boundary layers develop with distance from the leading edge and stay attached to the surfaces [Fig. 10(a)]. At $\tilde{A} = 1.6$, the laminar boundary layer on the upper surface exhibits a local

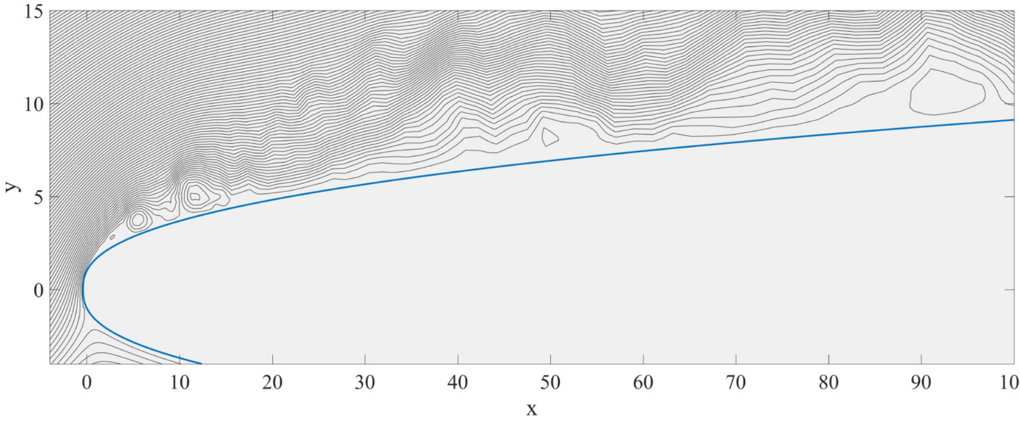

FIG. 7. The Ψ contour lines for the case with $a = 2.5$ (a $(2.5x^*)^{\frac{2}{5}}$ nose), $\mathrm{Re}_M = 900$, and $\tilde{A} = 1.5$ computed with the mesh $2M = 200$ by $N = 400$ at $t = 500$.

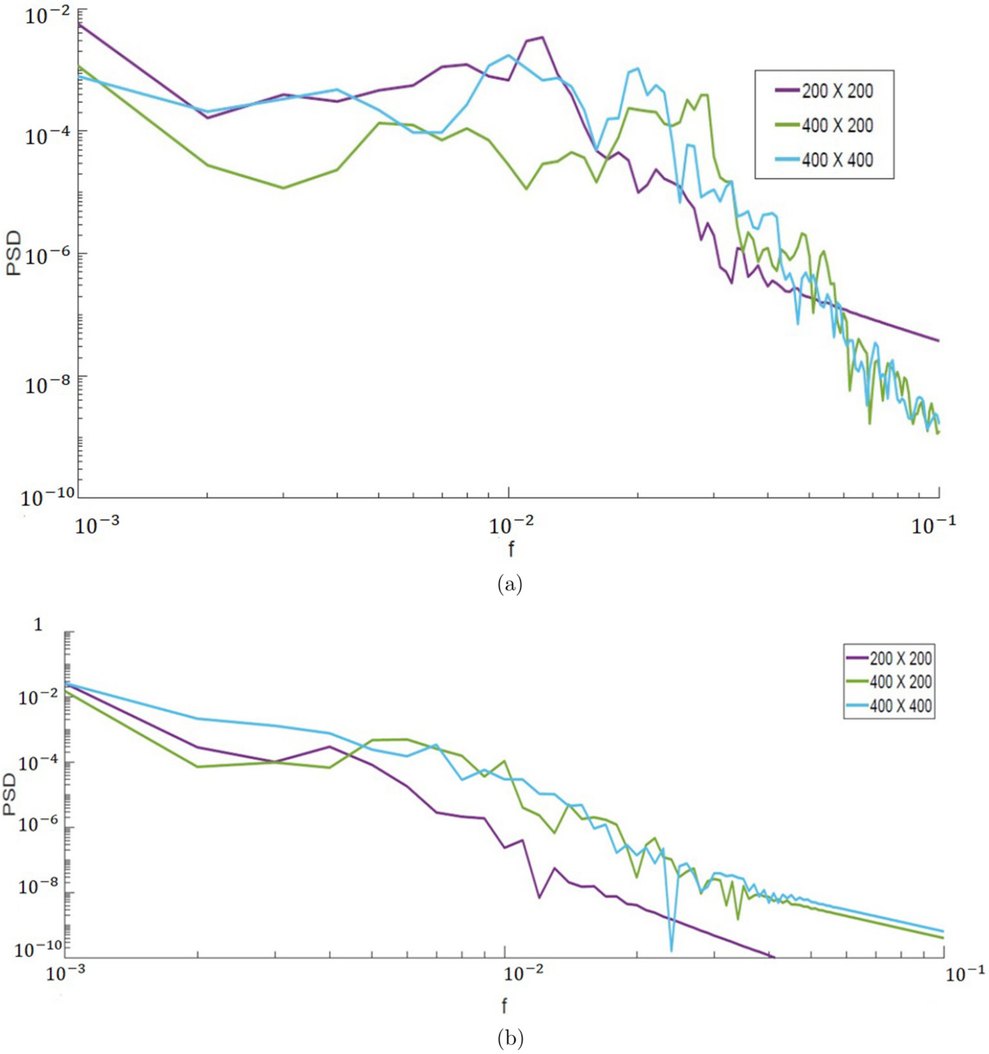

(a)

(b)

FIG. 8. Mesh refinement study of FFT results at long time flow behavior at $\mathrm{Re}_M = 900$ and $\tilde{A} = 1.5$ during the time interval $500 \leqslant t \leqslant 600$ from three meshes, $2M = 200$ by $N = 200$, $2M = 400$ by $N = 200$, and $2M = 400$ by $N = 400$ at points (a) $\mu = 2.6$, $\eta = 1.05$ and (b) $\mu = 6.6$, $\eta = 1.15$.

swelling around $x^* = 15$ and is on the verge of local separation [Fig. 10(b)]. At $\tilde{A} = 1.65$, a state of marginal separation, identified by a local laminar separation zone, appears in the boundary layer, centered around $x^* = 17$ [Fig. 10(c)]. As $\tilde{A}$ is further increased, the flow exhibits a global laminar separation zone when $\tilde{A}$ is greater than 1.7; see Figs. 10(d) for $\tilde{A} = 1.7$, 10(e) for $\tilde{A} = 1.75$, and 10(f) for $\tilde{A} = 1.8$. This indicates the leading-edge stall of an airfoil with a $x^{\frac{2}{5}}$ nose. For $a = 2.5$ and $\mathrm{Re}_M = 100$, we find that $\tilde{A}_s \sim 1.7$.

With the increase of Re_M from 100 to 600, the flow continues to exhibit a laminar boundary layer that swells with the increase of $\tilde{A}$ and eventually turns into a global laminar separation zone, similar to the results with $\mathrm{Re}_M = 100$. However, the onset of stall appears at a value of $\tilde{A}_s$ that decreases with Re_M. For example, at $\mathrm{Re}_M = 300$, we find that $\tilde{A}_s \sim 1.35$.

Computations of time-asymptotic states of flows at $\mathrm{Re}_M = 500$ around a nose with power $a = 2.5$ at various $\tilde{A}$ are shown in Fig. 11. At $\tilde{A} = 1.1$, the flow expands around the nose surfaces

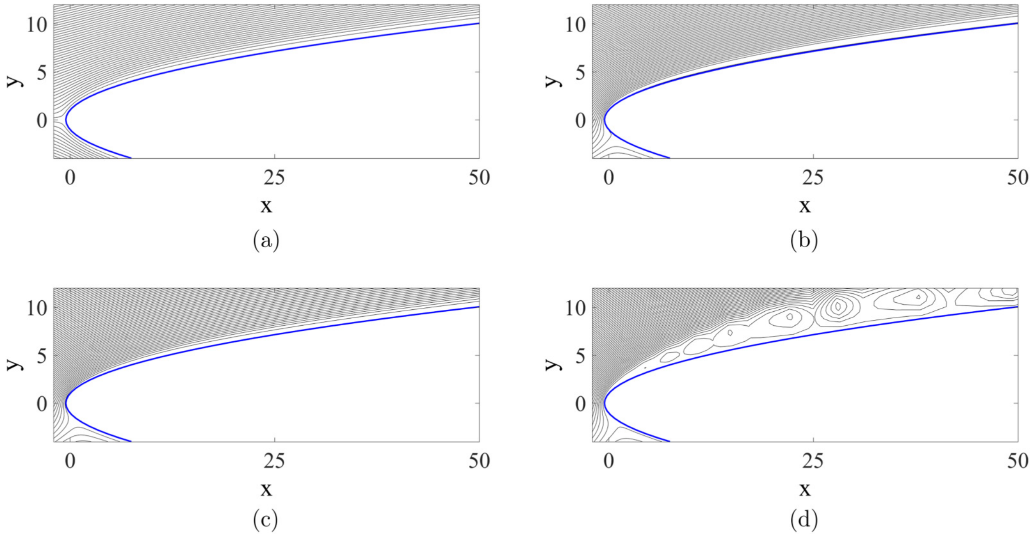

FIG. 9. Long-term states with $a = 2$ (a $(2x^*)^{\frac{1}{2}}$ nose), $\mathrm{Re}_M = 100$, and (a) $\tilde{A} = 0$, (b) $\tilde{A} = 1.3$, (c) $\tilde{A} = 1.4$, (d) $\tilde{A} = 1.77$.

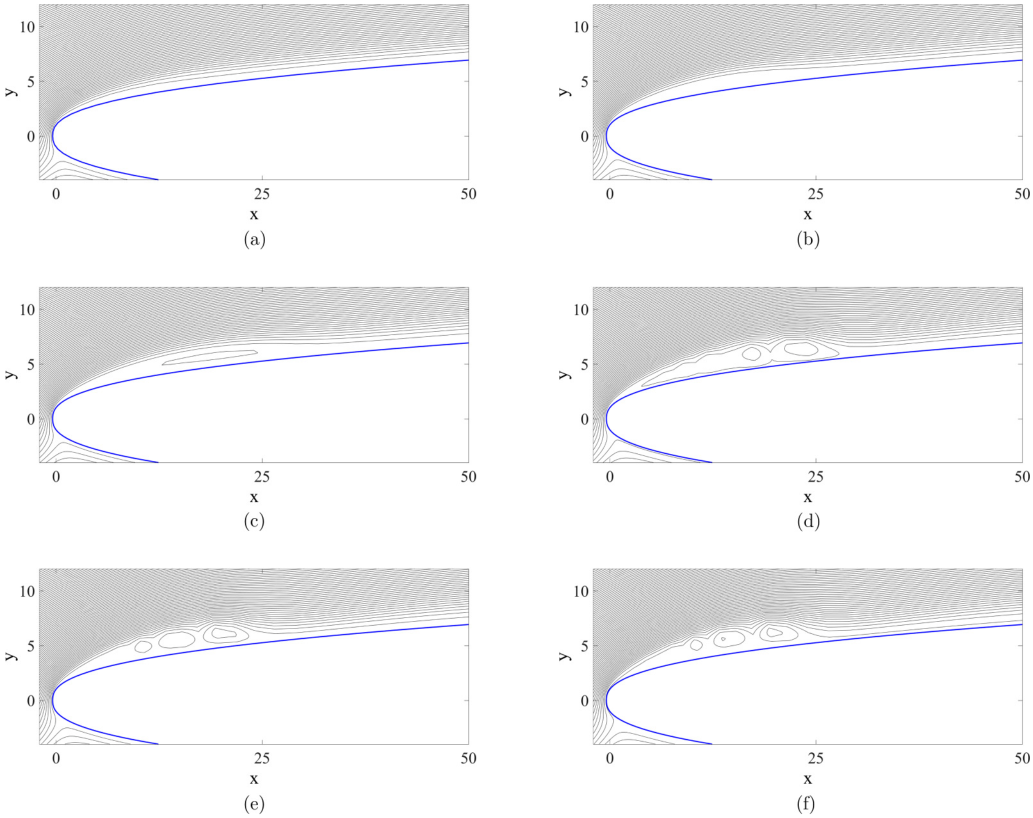

FIG. 10. Long-term states with $a = 2.5$ (a $(2.5x^*)^{\frac{2}{5}}$ nose), $\mathrm{Re}_M = 100$, and (a) $\tilde{A} = 1.5$, (b) $\tilde{A} = 1.6$, (c) $\tilde{A} = 1.65$, (d) $\tilde{A} = 1.7$, (e) $\tilde{A} = 1.75$, (f) $\tilde{A} = 1.8$.

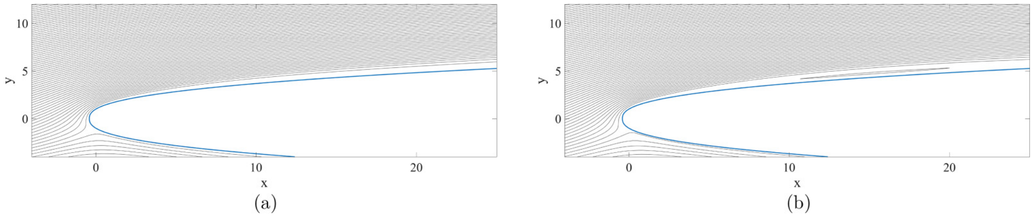

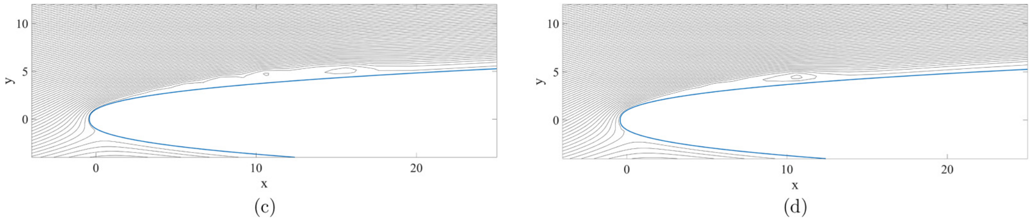

FIG. 11. Long-term states with $a = 2.5$ (a $(2.5x^*)^{\frac{2}{5}}$ nose), $\mathrm{Re}_M = 500$, and (a) $\tilde{A} = 1.1$, (b) $\tilde{A} = 1.2$, (c) $\tilde{A} = 1.3$, (d) $\tilde{A} = 1.4$.

and the laminar boundary layers develop with distance from the leading edge and stay attached [Fig. 11(a)]. At $\tilde{A} = 1.2$, the laminar boundary layer on the upper surface exhibits a local swelling around $x^* = 15$ and is on the verge of local separation [Fig. 11(b)]. At $\tilde{A} = 1.3$, flow separation occurs and the flow exhibits a global laminar separation zone [Fig. 11(c)], which continues to appear at values of $\tilde{A}$ above 1.3 [Fig. 11(d)]. For $a = 2.5$ and $\mathrm{Re}_M = 500$, we find that $\tilde{A}_s \sim 1.25$.

With the further increase of Re_M above 600, for a nose with $a = 2.5$, the flow exhibits a separation zone near the leading edge and the shedding of vortical waves from its tail. The waves are convected downstream along the upper surface. This situation is similar to the results found in Morris and Rusak [12] for the parabolic nose with $a = 2$ where unsteady flow behavior was found at $\mathrm{Re}_M > \mathrm{Re}_{M,\mathrm{lim}} = 300$. The flow unsteadiness in both cases ($a = 2$, $a = 2.5$) delays the onset of global separation and stall to higher values of $\tilde{A}_s$. For the nose with $a = 2.5$, we find that $\mathrm{Re}_{M,\mathrm{lim}} = 600$ for which a minimum $\tilde{A}_s$ is found, $\tilde{A}_s = 1.12$. Also, $\tilde{A}_s$ increases with the increase of $\mathrm{Re}_M > 600$. For example, when $\mathrm{Re}_M = 1\,000$, Fig. 12 describes the separated, unsteady flow state at $\tilde{A} = 1.7$ which is on the verge of stall as the maximum velocity on the upper surface continues to increase when $\tilde{A}$ is increased from lower values to 1.7. We find for $a = 2.5$ and $\mathrm{Re}_M = 1\,000$ that $\tilde{A}_s \sim 1.7$. Similarly, when $\mathrm{Re}_M = 1\,250$, we find that $\tilde{A}_s = 2.1$.

We conducted similar computations of the time-asymptotic states of flows around a nose with the power $a = 3$ at various Re_M and $\tilde{A}$. These computations show a behavior similar to that of

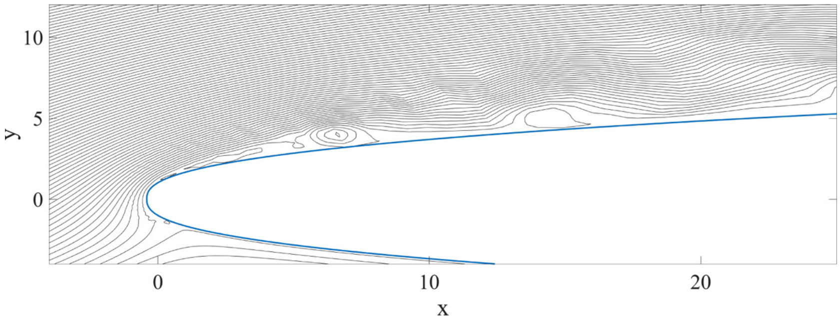

FIG. 12. Separated, unsteady flow state that is on the verge of global stall for a nose with $a = 2.5$ at $\mathrm{Re}_M = 1\,000$ and $\tilde{A} = 1.7$.

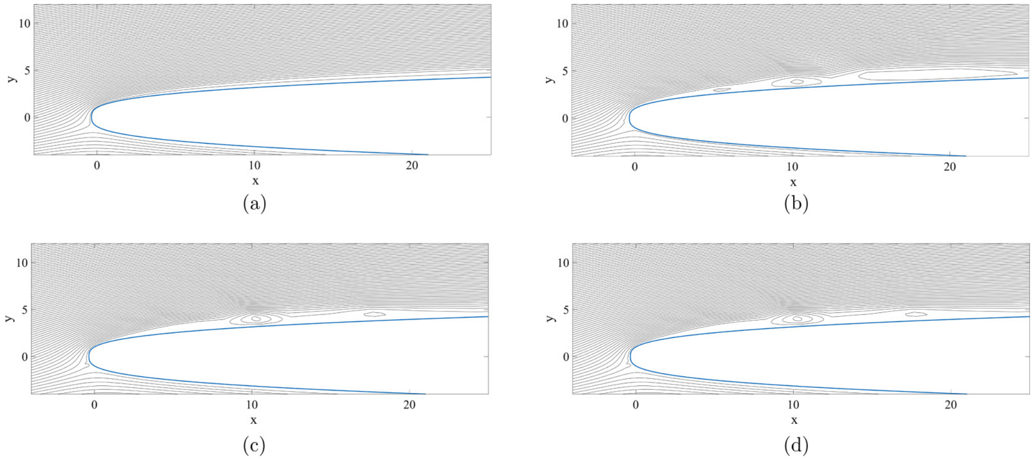

FIG. 13. Long-term states with $a = 3$ (a $(3x^*)^{\frac{1}{3}}$ nose), $\mathrm{Re}_M = 500$, and (a) $\tilde{A} = 0.9$, (b) $\tilde{A} = 1$, (c) $\tilde{A} = 1.1$, (d) $\tilde{A} = 1.2$.

flows around noses with powers $a = 2$ and $a = 2.5$. We find that for the $a = 3$ nose $\tilde{A}_s = 1.42$ at $\mathrm{Re}_M = 100$, it decreases with the increase of Re_M up to $\mathrm{Re}_{M,\lim} = 650$, where $\tilde{A}_s = 0.92$, and then increases with further increase of Re_M. For example, time-asymptotic flow contours at $\mathrm{Re}_M = 500$ are shown in Fig. 13. At $\tilde{A} = 0.9$, the flow expands around the nose surfaces and the laminar boundary layers develop with distance from the leading edge along the surfaces [Fig. 13(a)]. For $\tilde{A} \geqslant 1$, flow separation occurs and the flow exhibits a global laminar separation zone; see Figs. 13(b) for $\tilde{A} = 1$, 13(c) for $\tilde{A} = 1.1$, and 13(d) for $\tilde{A} = 1.2$. For $a = 3$ and $\mathrm{Re}_M = 500$, we find that $\tilde{A}_s \sim 0.95$.

The results for the values of $\tilde{A}_s$ at various values of Re_M, in the range between 100 and 1 250, and $a = 2,\ 2.5,\ 3$ are presented in Fig. 14. The figure shows that for the three values of a, the value of $\tilde{A}_s$ reaches a minimum value at a certain $\mathrm{Re}_{M,\lim}$ and then grows with the increase of $\mathrm{Re}_M > \mathrm{Re}_{M,\lim}$. This minimum of $\tilde{A}_s$ shifts to a higher value of $\mathrm{Re}_{M,\lim}$ as the value of a is increased. Also, the value of $\tilde{A}_s$ at the minimum point decreases with the increase of a.

Note, however, that both Re_M and $\tilde{A}_s$, given by Eqs. (18) and (23), are the rescaled Reynolds number and angle of attack, respectively, in terms of the nose characteristic length R_n/c, given by $R_n/c = a^{\frac{-1}{a-1}}(\delta h_0)^{\frac{a}{a-1}}$. As the nose parameter a gets higher, the nose becomes more blunt and R_n/c increases. Therefore, when the canonic results for $\tilde{A}_s(\mathrm{Re}_M; a)$ according to Fig. 14 are converted to compute the stall angle of an airfoil in the physical domain, the chord Reynolds number, $\mathrm{Re} = \mathrm{Re}_M/(R_n/c)$, is stretched less with the increase of a, while the stall angle, $\alpha_s(\mathrm{Re})$ according to Eq. (23), is stretched more with the increase of a. This may form results where the stall angle, α_s, of airfoils with various nose shapes is greater with the increase of a at a fixed Re. This behavior is demonstrated in the computed results of the following section.

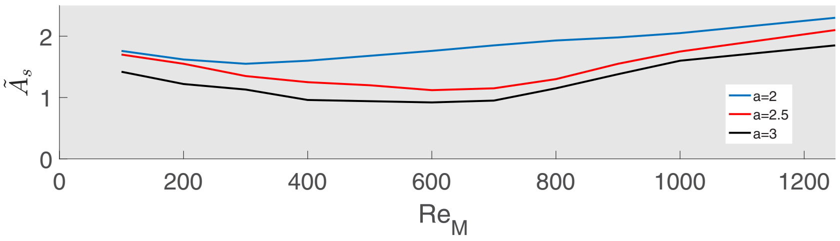

FIG. 14. Plot of $\tilde{A}_s$ for various values of Re_M and a.

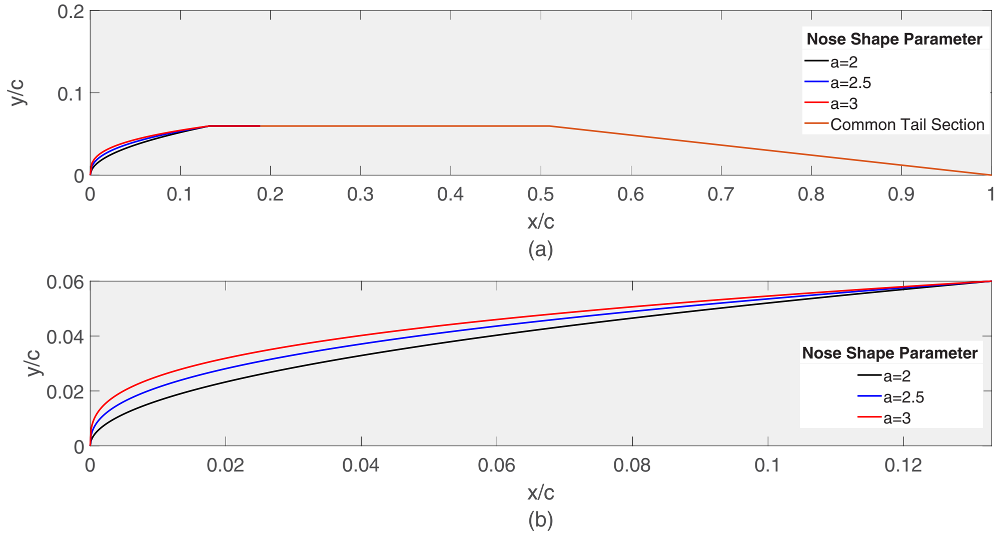

FIG. 15. (a) Example of symmetric airfoils with various noses, a common tail, and the same thickness ratio (0.12) with $x_t/c = 0.133$. (b) Magnified view of various nose geometries in the range $0 < x/c < x_t/c$.

Because of constraints on computational resources, the inner flow simulations are limited to $\mathrm{Re}_M \leqslant 1\,250$ to achieve numerically accurate results.

VI. EXTENSION OF STALL RESULTS TO HIGHER REYNOLDS NUMBERS

To extend the results of Sec. V to a stall prediction of $\tilde{A}_s$ at higher $\mathrm{Re}_M > 1\,250$, we used a Reynolds-averaged Navier-Stokes (RANS) solver to estimate the flow around canonic, symmetric airfoils with various nose shapes, a, and at various Re and angles of attack, α.

The studied airfoils were constructed in such a way that they all have the same thickness ratio of $\delta = 0.12$ but with various nose shapes $y = \pm k(a\frac{x}{c})^{\frac{1}{a}}$ in the range $0 \leqslant \frac{x}{c} \leqslant \frac{x_t}{c}$, where $k = \frac{\delta}{2}/(a\frac{x_t}{c})^{\frac{1}{a}}$. The nose is followed by a straight segment parallel to the x axis from $\frac{x_t}{c}$ to $\frac{x}{c} = 0.51$ and a common tail composed of straight lines connecting the end of the straight segment and the trailing edge at $\frac{x}{c} = 1$. The characteristic length of the nose is given by $R_n/c = (\delta/2)[t/(2ax_t)]^{1/(a-1)}$, where $t = \delta c$. See Fig. 15 for examples of symmetric airfoils with various noses, a common tail, and the same thickness ratio with a fixed $\frac{x_t}{c} = 0.133$. It can be seen that the noses of the airfoils become more blunt as a is increased above 2. Also, R_n/c increases with a.

The tested airfoils were designed to accommodate canonic noses with various values of a and $\frac{x_t}{c}$. The corner at $\frac{x}{c} = 0.51$ helps to anchor any trailing-edge separation that originates on the aft portion of the airfoil and prevent it from moving forward toward the leading edge. Thereby, the flow around the leading edge evolves in a natural way as the angle of attack is increased until a global leading-edge separation and stall occurs on the respective nose surface.

The commercially available software package ANSYS WORKBENCH was utilized with its geometry and mesh generation capabilities as well as its RANS flow solver, FLUENT. A nonuniform mesh of a C-shape domain surrounding each of the airfoils and extending to a control volume of 7.5 chord lengths ahead, behind, and normal to the surface of the airfoils was constructed using the integrated mesh construction software of the ANSYS suite. The mesh was weighted in both the normal and axial directions toward the surface of the airfoil and its nose in order to accurately capture the stagnation and maximum suction regions near the leading edge and the behavior of the flow in the viscous boundary layers over the surfaces of the airfoils. For a mesh with 276 000 elements in the domain

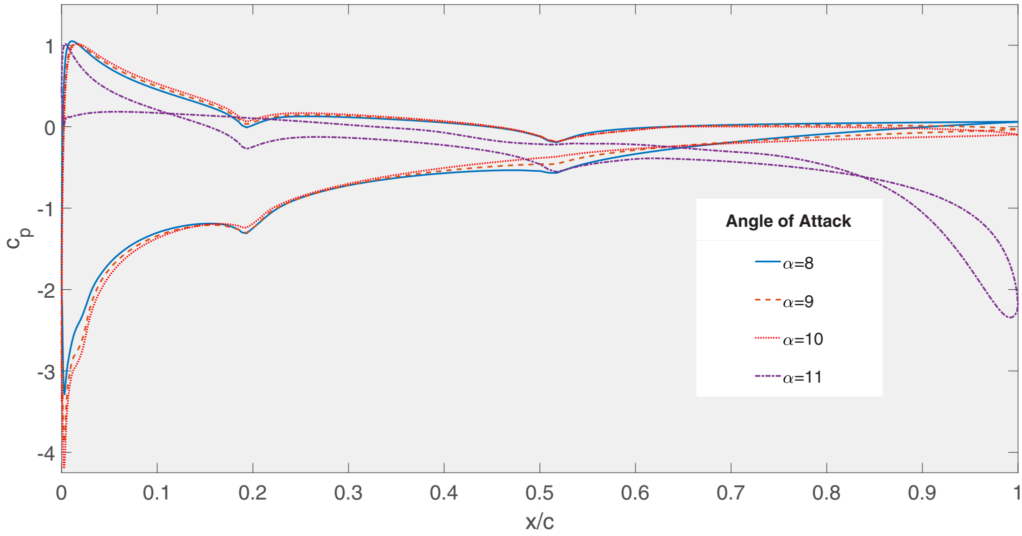

FIG. 16. The distribution of pressure coefficient, c_p, as a function of x/c for various angles of attack, $\alpha = 8^\circ, 9^\circ, 10^\circ, 11^\circ$ for an airfoil with $a = 2$ nose with maximum thickness at $x_t/c = 0.190$ and $\mathrm{Re} = 150\,000$. The stall of the airfoil is depicted as α increases form 10° to 11°.

around the airfoil, the typical element length near the leading edge is $1/700$ of the chord and in the boundary layer it is $1/150$ of the chord in the axial direction and $1/1\,400$ of the chord in the normal direction to the airfoil surface.

The airfoils were set in a uniform flow with a an upstream Mach number of $\mathrm{Ma} = 0.2$. The airfoil's geometry was scaled based on changing the chord length to provide operational conditions at various values of Re in the range $50\,000 \leqslant \mathrm{Re} \leqslant 300\,000$. The value of angle of attack, α, of the upstream flow was increased form zero in small increments for each Re value studied until a global stall occurred over the entire airfoil. On the downstream side of the control volume, the gauge pressure was set to zero. The no penetration and no slip conditions of the flow were set all along the surfaces of the airfoils. The $k - \omega$ turbulence model was used as part of the flow solver to describe the flow around the airfoils, particularly in the viscous boundary layer near the airfoil surfaces. Computed results exhibited, in the range of Re studied ($50\,000 \leqslant \mathrm{Re} \leqslant 300\,000$), little sensitivity of flow solutions to changes of the turbulence model parameters (see a similar demonstration by Morris [21]). The results of RANS computations also exhibit convergence with mesh refinement (see the study by Kraljic [22]).

At a fixed value of Re, the converged solution from a previous case of angle of attack was used as an initial solution for the next case of angle of attack until global separation and stall were observed. The determination of stall angle was based on the separation of flow from the upper surface of the airfoil as well as the sudden drop in value of the lift coefficient, c_l, and the sudden decrease in the magnitude of the minimum pressure coefficient on the airfoil, c_p.

Results for the airfoil representing the case of $a = 2$, $x_t/c = 0.190$, and $\mathrm{Re} = 150\,000$ are shown in Fig. 16. For this airfoil, $R_n/c = 0.0095$. As the angle of attack is increased from $\alpha = 8^\circ$ to $\alpha = 10^\circ$, the absolute magnitude of the minimum value of c_p increases. The plotting of the distribution of the pressure coefficient, c_p, for various α indicates a significant change in the absolute magnitude of the minimum c_p from 4.4 at $\alpha = 10^\circ$ to nearly zero at $\alpha = 11^\circ$. The computed results indicate the onset of a global leading-edge stall at $\alpha_s \sim 10.3^\circ$. The corresponding lift coefficient also drops significantly at this angle of attack.

The corresponding contours of velocity magnitude at various angles of attack are shown in Fig. 17 [Fig. 17(e) provides the velocity scale in meters per second] and also serve to indicate

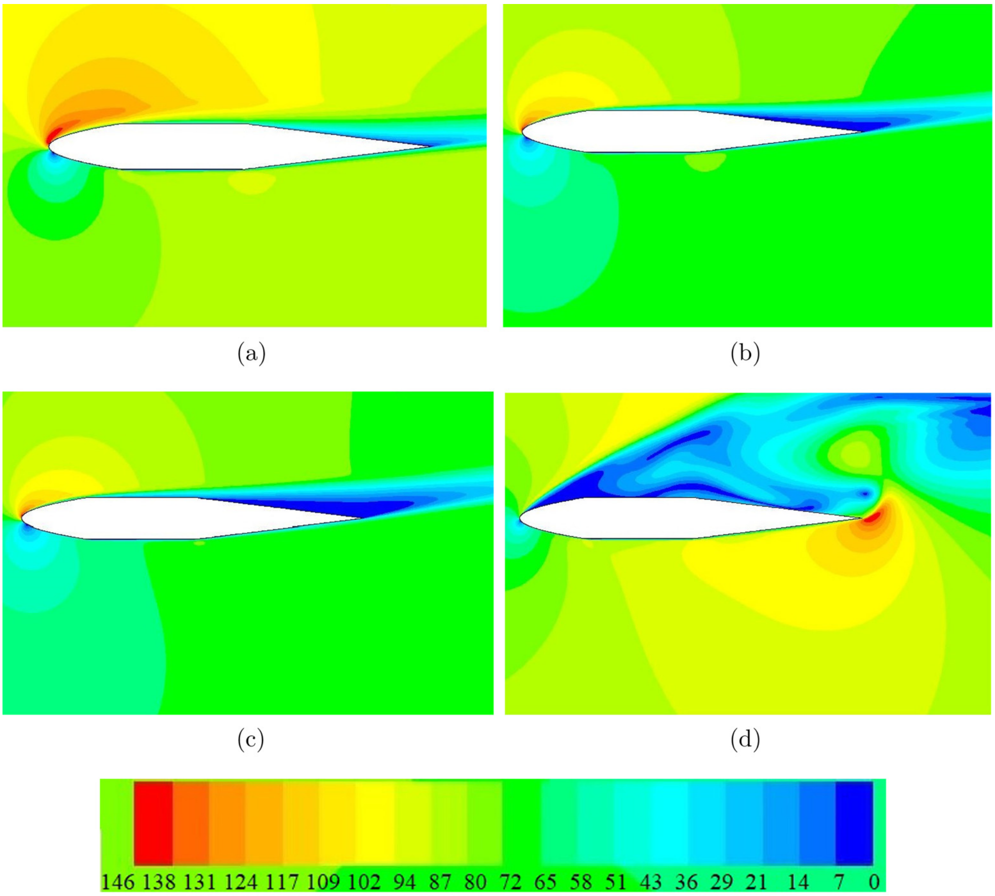

(a) (b) (c) (d) (e)

FIG. 17. The fields of velocity magnitude around the airfoil with $a = 2$, $x_t/c = 0.190$, $\mathrm{Re} = 150\,000$ at various angles of attack: (a) $\alpha = 8^\circ$; at this angle of attack, the flow is attached to both the lower and upper surfaces of the airfoil. (b) $\alpha = 9^\circ$; flow around most of the airfoil is attached but there is local flow separation near the trailing edge. (c) $\alpha = 10^\circ$; flow around most of the airfoil is attached but there is local flow separation near the trailing edge. (d) $\alpha = 11^\circ$; leading-edge stall state. (e) Velocity scale for parts (a) through (d) in meters per second.

the angle of stall of the airfoil. Figure 17(a) presents the contours of velocity magnitude for $\alpha = 8^\circ$ for which the flow is almost entirely attached to the surface of the airfoil. It exhibits the stagnation of the flow on the lower surface of the nose (the dark blue area), the region of high suction (the red area) with a maximum velocity up to 117 m/s on the upper surface of the nose, and the thin attached boundary layers (the blue lines along the surfaces of the airfoil). As α is increased through 9° and 10°, Figs. 17(b) and 17(c), the flow over the upper surface of the airfoil begins to gradually separate from the trailing edge of the airfoil forward. Further, the value of the maximum velocity over the surface of the airfoil increases (the red area) up to 141 and 146 m/s, respectively. The stagnation point also moves along the lower surface of the airfoil toward the trailing edge. Finally, as α is increased from 10° to 11°, Fig. 17(d), the flow suddenly and completely separates from the upper surface of the airfoil. The velocity of the flow above the airfoil becomes nearly stagnant and the stagnation point along the lower surface moves near to the leading edge of the airfoil. The airfoil is globally stalled in this state. This visual presentation is corroborated by the numerical results of

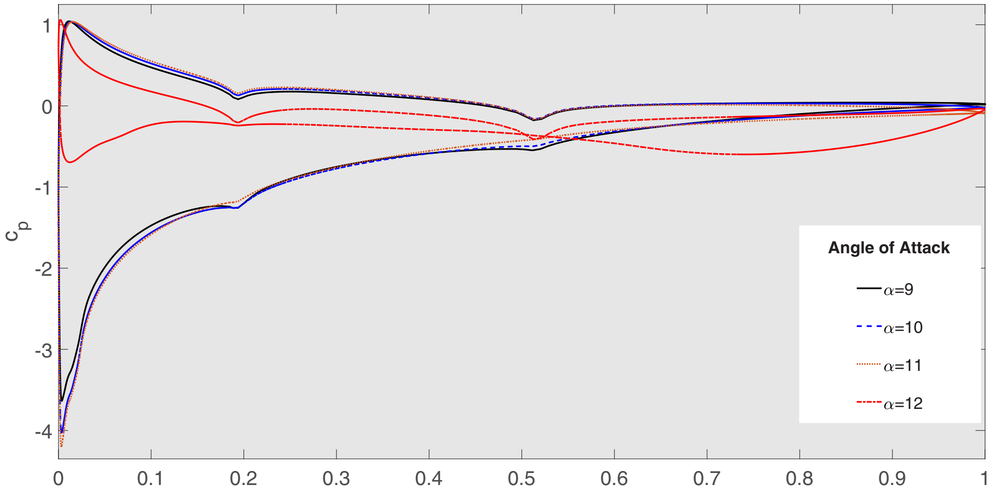

FIG. 18. The distribution of pressure coefficient, c_p, as a function of x/c for various angles of attack, $\alpha = 9^\circ, 10^\circ, 11^\circ, 12^\circ$ for an airfoil with $a = 2.5$ nose with maximum thickness at $x_t/c = 0.190$ and Re $= 150\,000$. The stall of the airfoil is depicted as α increases form 11° to 12°.

c_p presented above in Fig. 16. It should be noted that the stall of the airfoil in Fig. 17 describes a classical leading-edge stall phenomenon.

Results for an airfoil with a blunter nose of $a = 2.5$ and $x_t/c = 0.190$ at Re $= 150\,000$ are shown in Fig. 18. For this airfoil, $R_n/c = 0.0151$. Figure 18 presents the relationship between the distribution of c_p along the airfoil and α. As the angle of attack is increased up to 11°, the absolute magnitude of the minimum value of c_p increases to 4.2. When α is increased above 11°, the absolute magnitude of c_p suddenly drops to near-zero values and the airfoil is stalled. The results of Fig. 18 indicate the onset of a global leading-edge stall at $\alpha_s \sim 11.2^\circ$. The comparison of results in Figs. 16 and 18 shows that the stall angle increases with the increase of the nose bluntness (increase of the nose parameter a and the related R_n/c).

Contours of velocity magnitude at various angles of attack are shown in Fig. 19 [Fig. 19(d) provides the velocity scale in meters per second] and support the stall prediction from Fig. 18. Figure 19(a) presents the contours of velocity magnitude for $\alpha = 9^\circ$ for which the flow is almost entirely attached to the surface of the airfoil and the peak velocity is 134 m/s. As α is increased through 10° and 11°, as shown in Figs. 19(b) and 19(c), the flow over the upper surface of the airfoil begins to gradually separate from the trailing edge of the airfoil forward. Yet, the value of the maximum velocity over the surface of the airfoil increases (the red areas) to 142 m/s as the nose region continues to build suction and lift. The stagnation point also moves along the lower surface of the airfoil toward the trailing edge. As α is increased to 12°, the flow suddenly and completely separates from the upper surface of the airfoil and the airfoil stalls. The velocity of the flow above the airfoil becomes nearly stagnant and the stagnation point moves near to the leading edge of the airfoil. The comparison of Figs. 17 (for a nose with $a = 2$) and 19 (for a nose with $a = 2.5$) demonstrates again the increase of leading-edge stall angle as a is increased from 2 to 2.5.

The RANS computations were repeated for various values of the nose-shape parameter, a, in the range $2 \leqslant a \leqslant 3$, and Re in the range $50\,000 \leqslant \text{Re} \leqslant 300\,000$. The results of the computations were used to continue the prediction of $\tilde{A}_s$ to values of Re_M above those which were studied by the direct numerical simulations of Sec. V. By using Eq. (23), the results of the RANS computations for $\alpha_s(\text{Re})$ were converted to values of $\tilde{A}_s(\text{Re}_M; a)$. For the airfoils with a nose shape parameter of $a = 2$ and with $x_t/c = 0.133$ and $x_t/c = 0.190$, the results of the RANS computations, in the form of $\tilde{A}_s$ as a function of Re_M, are plotted (dotted lines) in Fig. 20 along with the results of the direct numerical simulation (solid line) for $a = 2$. It is noteworthy that the RANS results for the

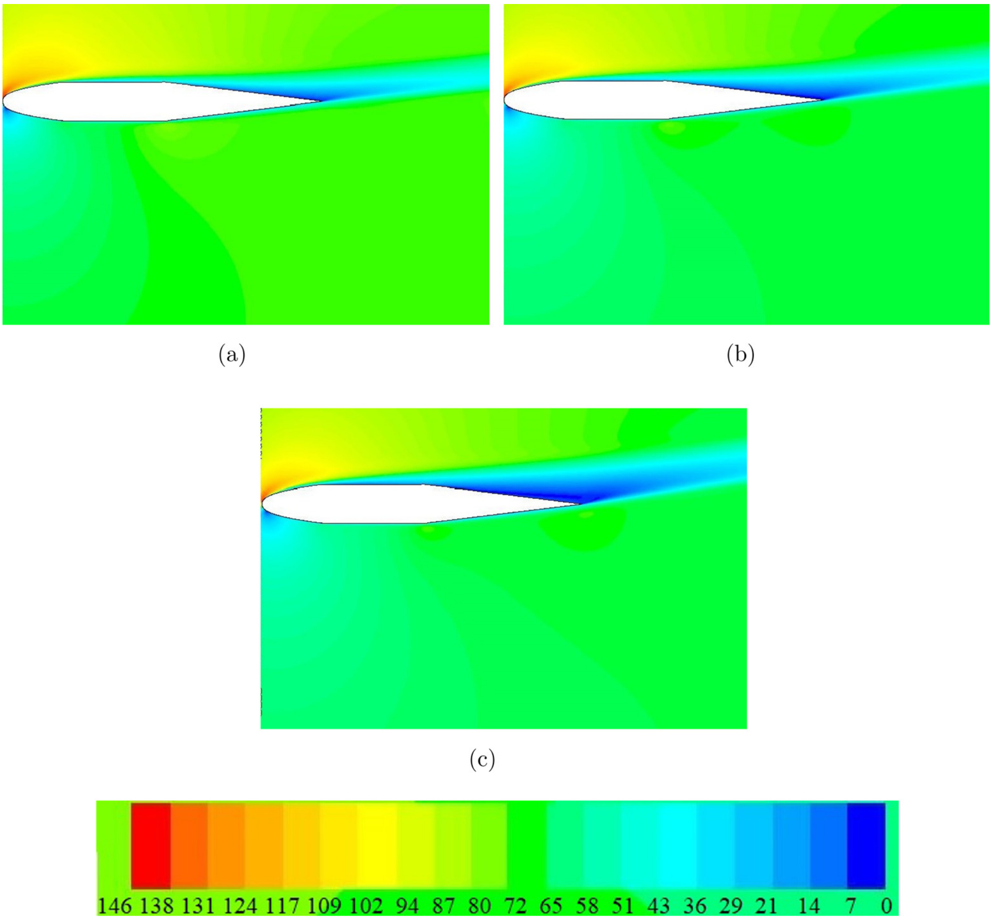

(a) (b)

(c)

(d)

FIG. 19. The fields of velocity magnitude around the airfoil with $a = 2.5$, $x_t/c = 0.190$, $\mathrm{Re} = 150\,000$ at various angles of attack: (a) $\alpha = 9^\circ$; at this angle of attack, the flow is slightly separated near the trailing edge. (b) $\alpha = 10^\circ$; flow around most of the airfoil is attached but there is local flow separation near the trailing edge. (c) $\alpha = 11^\circ$; flow around most of the airfoil is attached but there is local flow separation near the trailing edge. (d) Velocity scale for parts (a) through (c) in meters per second.

cases of $x_t/c = 0.133$ and $x_t/c = 0.190$ are nearly identical (within computational error limits) in terms of $\tilde{A}_s(\mathrm{Re}_M)$ for $\mathrm{Re}_M > 800$. This suggests that changes in x_t/c have no measurable impact on the value of the universal stall prediction, $\tilde{A}_s(\mathrm{Re}_M; a)$. Moreover, Fig. 20 shows that in the lower range of Re_M up to $\mathrm{Re}_M = 1\,250$ the results from the direct numerical simulation are valid and represent the angle of stall of the airfoil. In the range of $\mathrm{Re}_M \geqslant 800$, the results of the RANS computations are relevant and also represent the stall angle of the airfoil. There exists a range of Re_M ($800 \leqslant \mathrm{Re}_M \leqslant 1\,250$) where there is an overlap between the results of the direct numerical simulation and the RANS computations.

In a similar fashion, Fig. 21 depicts the results for the airfoils with a nose shape parameter $a = 2.5$ in the form of $\tilde{A}_s$ as a function of Re_M. In this case, there again exists a region for which the results of the direct numerical simulation (the solid line) are valid ($\mathrm{Re}_M \leqslant 1\,250$) and a region for which the RANS computations (the dotted line) are valid ($\mathrm{Re}_M > 1\,400$). Further, there exists a region of Re_M for which results of the direct numerical simulation have been extrapolated from the existing data into the range $1\,250 \leqslant \mathrm{Re}_M \leqslant 1\,750$ (the dashed line). The region of Re_M

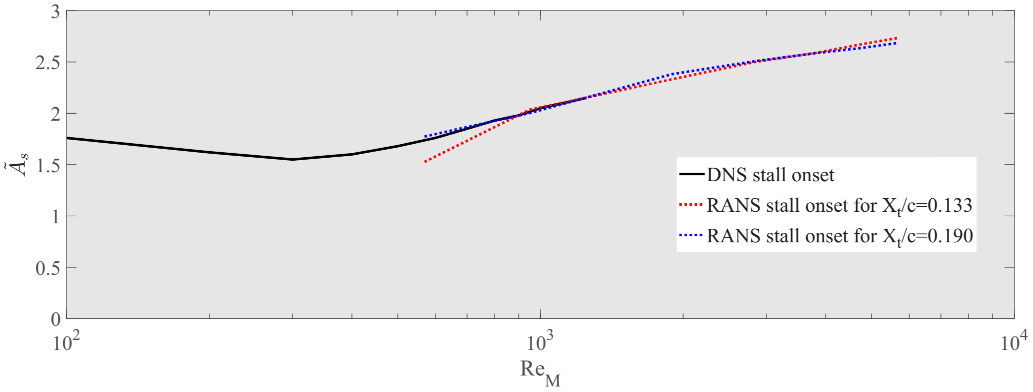

FIG. 20. $\tilde{A}_s$ as a function of Re$_M$ for an airfoil with a nose shape parameter of $a = 2$. The solid line represents the results of the direct numerical simulations. The dashed line represents the results extrapolated from the existing direct numerical simulation results. The dotted lines represent the results of the RANS computations for various values of x_t/c. Note that the RANS computations represent a continuation of the results of the direct numerical simulation to higher values of Re$_M$. Also note that the value of x_t/c does not have an impact on $\tilde{A}_s$(Re$_M$).

values between $1\,400 \leqslant \text{Re}_M \leqslant 1\,750$ represents expected overlap between the results of the direct numerical simulation and the RANS computations.

A plot of $\tilde{A}_s$ as a function of Re$_M$ for airfoils with a nose shape parameter of $a = 3$ is shown in Fig. 22. Here again there exist regions of validity for the direct numerical simulation ($100 \leqslant \text{Re}_M \leqslant 1\,250$), for the RANS computation ($\text{Re}_M \geqslant 2\,000$) and an overlap region between the extrapolated numerical simulation results (dashed line) and the RANS results ($2\,000 \leqslant \text{Re}_M \leqslant 2\,500$).

The results of $\tilde{A}_s(\text{Re}_M; a)$ from Figs. 20 and 21 were used to compute values of $\alpha_s(\text{Re})$ for the various airfoils in Fig. 15. These results are plotted in Fig. 23 ($a = 2.5$) for various values of x_t/c. Also shown in this figure are the computed angles of attack of stall of the airfoils from the RANS computations. It can be seen that the RANS computations slightly overpredict the predictions using $\tilde{A}_s(\text{Re}_M; a)$ (by about half a degree for $\text{Re} > 100\,000$) but have the same trend of increasing α_s with the increase of Re. Moreover, the figure shows that as the position of the maximum thickness, x_t/c,

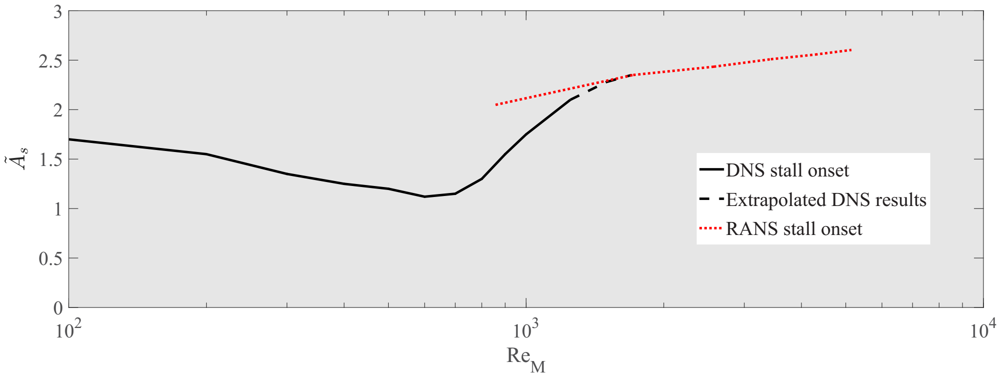

FIG. 21. $\tilde{A}_s$ as a function of Re$_M$ for an airfoil with a nose shape parameter of $a = 2.5$. The solid line represents the results of the direct numerical simulations. The dashed line represents the results extrapolated from the existing direct numerical simulation results. The dotted line represents the results of the RANS computations. Note that the RANS computations represent a continuation of the results of the direct numerical simulation to higher values of Re$_M$.

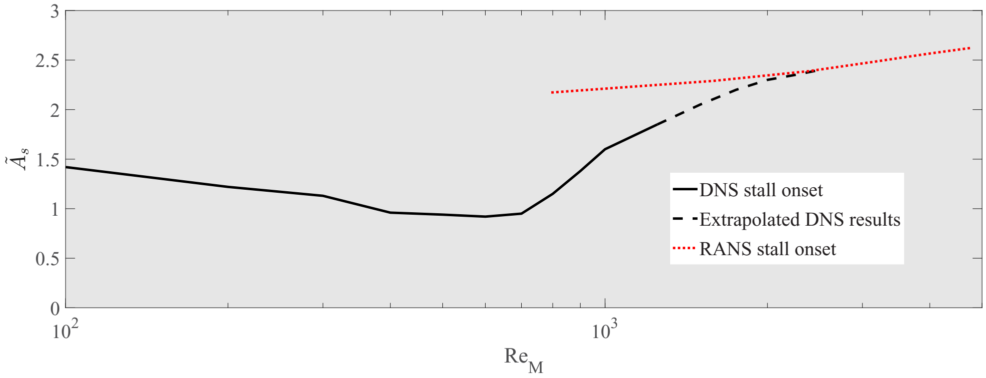

FIG. 22. $\tilde{A}_s$ as a function of Re_M for an airfoil with a nose shape parameter of $a = 3$. The solid line represents the results of the direct numerical simulations. The dashed line represents the results extrapolated from the existing direct numerical simulation results. The dotted line represents the results of the RANS computations. Note that the RANS computations represent a continuation of the results of the direct numerical simulation to higher values of Re_M.

is moved closer to the leading edge α_s increases. In a similar way, Fig. 24 describes the change in stall angle of attack, α_s, for airfoils with various values of the nose-shape parameter, a, and a fixed value of $\frac{x_t}{c} = 0.190$. The figure indicates a general decrease of α_s for all Re below a certain $\mathrm{Re}_{\mathrm{lim}}$, which increases with the nose-shape parameter, a. Above this value of $\mathrm{Re}_{\mathrm{lim}}$, the angle of attack of stall increases with Re. Furthermore, the results indicate that for $\mathrm{Re} > \mathrm{Re}_{\mathrm{lim}}$ the value of α_s increases with the increase of the nose-shape parameter a.

A comparison of the present theoretical predictions of the leading-edge stall angle of attack with RANS computations for the classical NACA 0012 airfoil are shown in Fig. 25(a). It can be

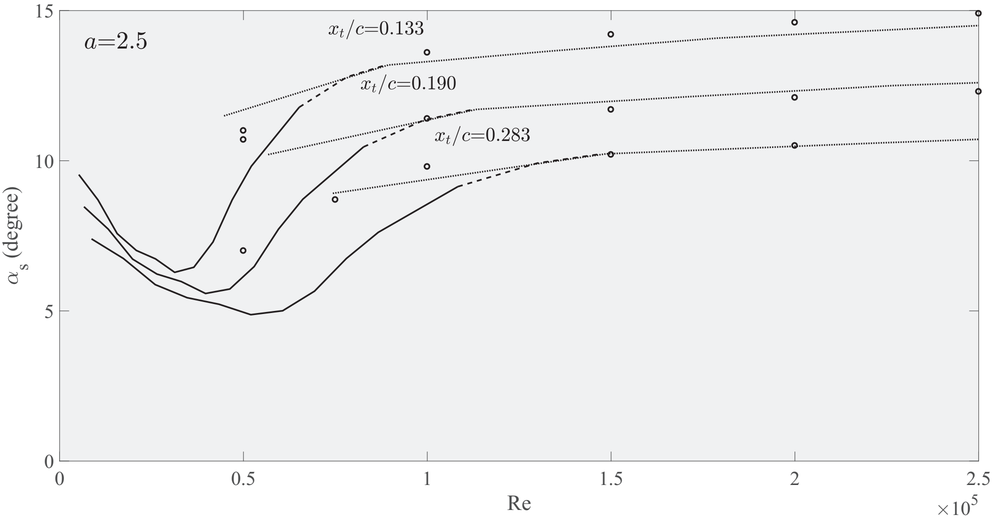

FIG. 23. Leading-edge stall angle vs Reynolds number for an airfoil with a nose shape parameter of $a = 2.5$ and various values of x_t/c. Note that as x_t/c is increased, the angle of stall decreases. The solid lines represent the results of direct numerical simulations. The dashed lines are from extrapolated results of the direct numerical simulations. The dotted lines represent predictions from RANS computations. The circles represent the RANS results.

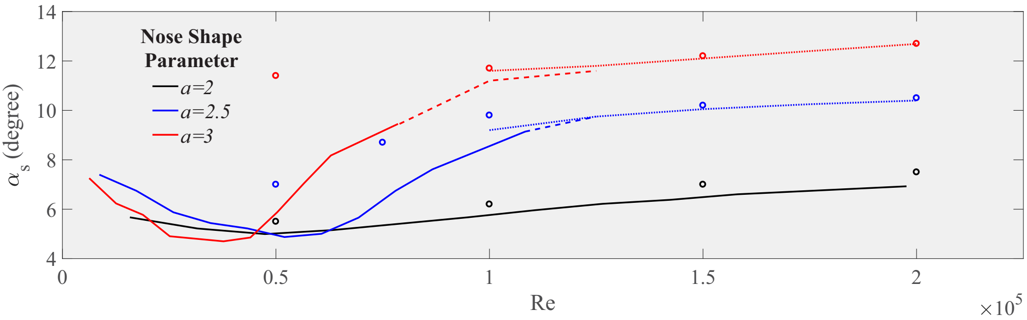

FIG. 24. Leading-edge stall angle vs Reynolds number for an airfoil with a fixed value of $x_t/c = 0.190$ and various a. Note that as a is increased, the angle of stall increases. The solid lines represent the results of direct numerical simulations. The dashed lines are from extrapolated results of the direct numerical simulations. The dotted lines represent predictions from RANS computations. The circles represent the RANS results.

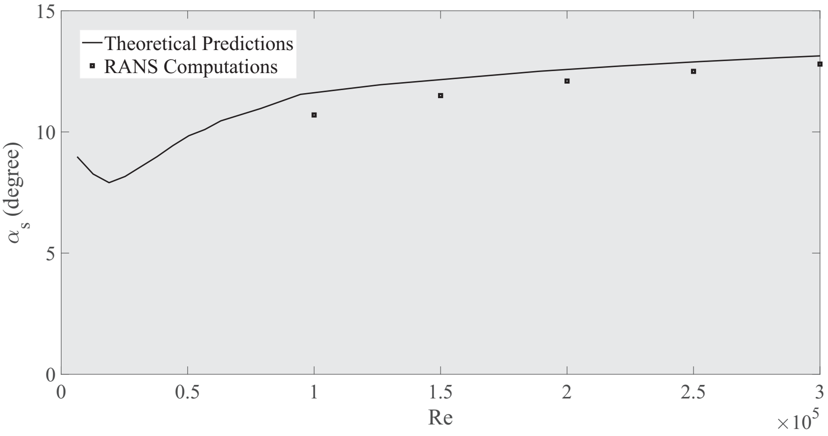

(a)

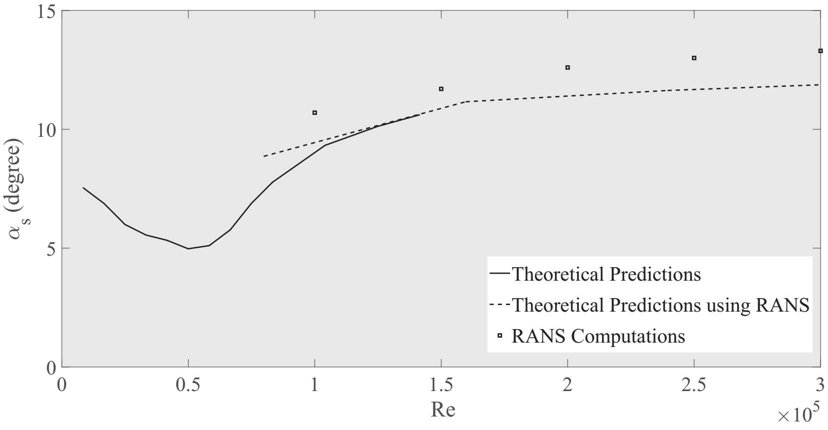

(b)

FIG. 25. Comparison of theoretical predictions with RANS computations of the leading-edge stall angle of attack for (a) the NACA 0012 airfoil and (b) a special transonic airfoil design.

seen that the predictions and the RANS computations agree within half a degree for $\mathrm{Re} > 100\,000$ and both increase with the increase of Re. In addition, we also studied the leading-edge stall properties of a specially designed transonic airfoil for a high critical Mach number by Rusak and Lee [23] which has an $x^{(2/5)}$ nose. The shape function of this symmetric airfoil is given by $y/c = \delta[0.8469(x/c)^{2/5} - 0.2645(x/c) + 1.3018(x/c)^2 - 3.6896(x/c)^3 + 1.8054(x/c)^4]$. A comparison of the present theoretical predictions with RANS computations for the leading-edge stall of this airfoil (with $\delta = 0.12$) is presented in Fig. 25(b). It can be seen that the predictions and the RANS computations agree within 1 deg for $\mathrm{Re} > 100\,000$. In comparison to the NACA 0012 airfoil, this airfoil results in both a higher stall angle of attack by half a degree as well as an increased critical Mach number by 0.03 at both 0- and 1-deg angles of attack [21]. This example demonstrates the ability to design airfoils with blunter than classical noses that exhibit both higher stall angles of attack and higher critical Mach numbers. Such airfoils may be used in the design of rotor blades operating at high rotational speeds as well as high forward-flight speeds.

VII. SUMMARY AND CONCLUSIONS

A. Summary of results

We studied the dynamics of viscous and incompressible flows around thin airfoils with blunter than classical noses at low to moderately high chord Reynolds numbers (Re) via an asymptotic analysis and numerical simulations. The objective is to theoretically show that blunter noses delay the onset of leading-edge stall to higher angles of attack by determining the angle of attack of leading-edge stall inception of the airfoil as a function of upstream-flow Reynolds number and airfoil nose geometry.

A reduced-order, multiscale model problem is developed and complemented by numerical computations. The asymptotic theory demonstrates that the flow about a thin airfoil can be described in terms of an outer region, around most of the airfoil's chord, and an inner region, around the nose, that asymptotically match each other in an intermediate overlap region. The flow in the outer region is dominated by the classical thin airfoil theory and shows a singular behavior near the leading edge. To fix this behavior, there is a need for an analysis of the flow around the nose by way of an inner region. Scaled (magnified) coordinates and a modified (smaller) Reynolds number [$\mathrm{Re}_M = \mathrm{Re}(R_n/c)$] are used to correctly account for the nonlinear behavior and acute velocity changes in the inner region. The far field of the inner region is described by a symmetric effect due to nose shape and an asymmetric effect with a lumped circulation parameter, $\tilde{A}$, due to angle of attack and camber. The asymptotic theory shows that the symmetric effects around the nose become more dominant than the circulation effects as the nose shape parameter, a, is increased from the classical value of 2 (parabolic noses). Therefore, it is expected that flow separation and global stall are delayed to higher angles of attack.

The inner flow problem is solved numerically using a transformation from the physical domain to a computational domain and a second-order finite-difference scheme for integrating the vorticity and stream function. The computed results demonstrate numerical convergence with mesh refinement. The inner-region solutions reveal the nature of the flow dynamics around the nose and the first inception of global stall as $\tilde{A}$ is increased above a certain value, $\tilde{A}_s$, at a fixed Re_M. The inner flow simulations result in Fig. 14 which provides the details of computed $\tilde{A}_s$ as a function of Re_M for noses with powers $a = 2$, 2.5, and 3. For each a, there exists a limit modified Reynolds number, $\mathrm{Re}_{M,\mathrm{lim}}$, where $\tilde{A}_s$ reaches a minimum value. The value of $\mathrm{Re}_{M,\mathrm{lim}}$ increases with the increase of a. For $\mathrm{Re}_M < \mathrm{Re}_{M,\mathrm{lim}}$ the value of $\tilde{A}_s$ decreases with the increase of Re_M from small values to $\mathrm{Re}_{M,\mathrm{lim}}$. At values of $\mathrm{Re}_M > \mathrm{Re}_{M,\mathrm{lim}}$, the value of $\tilde{A}_s$ increases with the increase of Re_M.

Because of constraints on computational resources, the inner flow simulations are limited to $\mathrm{Re}_M \leqslant 1\,250$ to achieve numerically accurate results. In order to extend the results of $\tilde{A}_s$ to higher values of Re_M, a Reynolds-averaged Navier-Stokes (RANS) solver was utilized to simulate the flow around symmetric airfoils with various canonic noses. The results of the inner flow simulations overlap with the RANS results in a certain range of Re_M, thereby providing a continuous universal stall prediction line from low to high Re_M. Figures 20–22 provide the prediction of the universal stall circulation parameter, $\tilde{A}_s$, for $a = 2, 2.5$, and 3, respectivley, in a range of Re_M between 100 and 4 000.

Note, however, that both Re_M and $\tilde{A}_s$, given by Eqs. (18) and (23), are re-scaled Reynolds number and angle of attack, respectively, in terms of the nose characteristic length R_n/c. As the nose parameter a becomes higher, the nose becomes more blunt and R_n/c increases. Therefore, when the canonic results for $\tilde{A}_s(\mathrm{Re}_M; a)$ are converted to compute the stall angle of an airfoil in the physical domain, the Reynolds number, $\mathrm{Re} = \mathrm{Re}_M/(R_n/c)$, is stretched less with the increase of a, while the stall angle, $\alpha_s(\mathrm{Re})$ according to Eq. (23), is stretched more with the increase of a. This forms results where the stall angle, α_s, of airfoils with various nose shapes is greater with the increase of a at a fixed Re. The results of $\tilde{A}_s$ as a function of Re_M and a are used to determine the stall angle of attack of the various airfoils, α_s as a function of Re. Figures 23–25 demonstrate the agreement between the theoretically predicted results for leading-edge stall and the RANS simulations for various airfoils including the NACA 0012 (with a parabolic nose) and a specially designed transonic airfoil (with an $x^{2/5}$ nose).

B. Conclusions

The research summarized above results in the following conclusions:

(1) The onset of leading-edge stall of thin airfoils with various blunt noses can be analyzed by a matched asymptotic analysis and numerical simulations using a finite-difference formulation of the inner region problem, at low to moderately high Re and RANS computations at higher Re.

(2) A universal prediction of the stall onset parameter, $\tilde{A}_s$, as a function of the modified Reynolds number, Re_M, and nose-shape parameter, a, is developed in Figs. 20–22.

(3) The predictions show agreement with computations of stall onset of airfoils using the RANS solver.

(4) The stall angle of airfoils increases with the increase of the nose parameter, a, or the decrease of the maximum thickness position, x_t/c. Both effects increase the value of R_n/c and, therefore, the nose bluntness.

The results are limited to thin, two-dimensional airfoils with thickness ratios of no more than 12% and camber ratios up to 4%. For thicker and more cambered airfoils, trailing-edge stall may dominate the airfoil's stall behavior. Note that high subsonic speed systems, including general aviation and commercial aircraft as well as turbine and compressor blades of engines and power generators, commonly use airfoils with thickness ratios equal to or less than 12%, where the present results may be applicable for these airfoils during operation at low subsonic speeds and high angle of attack.

In addition, the increase of nose bluntness to delay the onset of stall to higher angles of attack may result in some increase of the airfoil drag at lower angles of attack. However, in the typical design of aerodynamic systems, this increase of viscous drag may be less crucial than the resulting higher stall angle and wider range of angle-of-attack operation.

The results are also limited to moderately high upstream-flow Reynolds numbers up to $\mathrm{Re} = 300\,000$. The extension of results to higher Reynolds numbers requires the use of more capable computational resources.

We note that transonic airfoils with the highest critical Mach number also exhibit blunt noses with $a = 2.5$; see the studies of Schwendeman *et al.* [24] and Rusak [25,26], who established analytically the increase of critical Mach number for airfoils with blunt noses ($a = 2/5$) or even with a short straight vertical segment at the leading edge (Kropinski *et al.* [27]). This increase of critical Mach number may be of the order of 0.03 with respect to classical parabolic nose airfoils. This suggests that airfoils with blunt noses, with $a > 2$, may perform better than classical parabolic nose airfoils at both low-speed, high-lift flight conditions and at low-lift, transonic flight conditions. For example, such airfoils may be used in the design of helicopter rotors that may have the same airfoil section and experience low-speed, high-lift conditions on the retreating side and transonic speed, low-lift conditions on the advancing side of rotor rotation in forward flight. Future work in connection with this issue may focus on the study of the transonic characteristics of blunter nose airfoils as well as optimization studies to determine airfoil shapes which balance transonic performance with low-speed, high-angle-of-attack performance.

An extension of the present study to determine the onset of leading-edge stall on finite wings or blades of high aspect ratio is also needed. Such an approach may use an asymptotic study that builds on the interaction between the finite, high-aspect-ratio wing theory of Prandtl and the local, wing section stall behavior as described in the present study. Specifically, the idea is to include the downwash effect of the vortex wake behind the wing in the lumped circulation parameter $\tilde{A}$ and thereby form a study that will provide the stall onset values, $\tilde{A}_s$ in terms of Reynolds number, Re_M, nose shape parameter, a, and wing shape (leading-edge sweep angle, aspect ratio, and taper ratio). Such a challenging study may provide a theoretical foundation for the empirical techniques used to determine stall angle described in Raymer [28]. It may also explain the experimental findings of wing shape and sweep angle effects on the stall behavior in Yen and Huang [6].

APPENDIX: NUMERICAL METHODOLOGY FOR THE SOLUTION OF THE INNER PROBLEM

1. Numerical scheme of the solution

For the numerical implementation of the solution of Eqs. (38) and (31), the semi-infinite domain, $-\infty < \mu < \infty$ and $\eta \geqslant 1$, is reduced to the computational domain, $-\mu_{\max} \leqslant \mu \leqslant \mu_{\max}$ and $1 \leqslant \eta \leqslant \eta_{\max}$, where $\mu_{\max}$ and $\eta_{\max}$ are sufficiently large. The domain is discretized by a uniform mesh with equal spacing in both directions given by $\Delta\mu = \frac{\mu_{\max}}{M}$ and $\Delta\eta = \frac{\eta_{\max}}{N}$, where the indices of each grid point in the domain are given by (i, j) and $1 \leqslant i \leqslant 2M+1$, $1 \leqslant j \leqslant N+1$. Then, the coordinates of each grid point are $\mu_{ij} = [i-(M+1)]\Delta\mu$ and $\eta_{ij} = 1 + (j-1)\Delta\eta$. Time is discretized by constant time steps denoted as $\Delta\tau^*$ with index n for each time step. The time derivative in the vorticity transport equation, (38), is approximated by an explicit first-order forward difference. The spatial derivatives are approximated by second-order central differences.

Let

$$s_{ij} = \sqrt{\mu_{ij}^a + \eta_{ij}^a}, \tag{A1}$$

$$q_{ij} = \sqrt{\mu_{ij}^{2(a-1)} + \eta_{ij}^2}, \tag{A2}$$

$$p_{ij} = \sqrt{\mu_{ij}^2 + \eta_{ij}^{2(a-1)}}. \tag{A3}$$

The discretized formulation of the vorticity transport equation is then given by [with Eqs. (32)–(36)]

$$\begin{aligned}
&\frac{\omega_{i,j}^{n+1} - \omega_{i,j}^n}{\Delta\tau^*} + \frac{1}{s_{ij}^2}\left[\frac{q_{i+1,j}V_{\mu i+1,j}^n\omega_{i+1,j}^n - q_{i-1,j}V_{\mu i-1,j}^n\omega_{i-1,j}^n}{2\Delta\mu}\right]\\
&\quad + \frac{1}{s_{ij}^2}\left[\frac{p_{i,j+1}V_{\mu i,j+1}^n\omega_{i,j+1}^n - p_{i,j-1}V_{\mu i,j-1}^n\omega_{i,j-1}^n}{2\Delta\eta}\right]\\
&= \frac{1}{\mathrm{Re}_M}\left[\frac{\omega_{i+1,j}^n - 2\omega_{ij}^n + \omega_{i-1,j}^n}{(\Delta\mu)^2}K_{ij} + \frac{\omega_{i,j+1}^n - 2\omega_{ij}^n + \omega_{i,j-1}^n}{(\Delta\eta)^2}L_{ij}\right.\\
&\quad + 2\frac{\omega_{i+1,j+1}^n - \omega_{i+1,j-1}^n - \omega_{i-1,j+1}^n + \omega_{i-1,j-1}^n}{4\Delta\mu\Delta\eta}M_{ij}\\
&\quad \left. + \frac{\omega_{i+1,j}^n - \omega_{i-1,j}^n}{2\Delta\mu}N_{ij} + \frac{\omega_{i,j+1}^n - \omega_{i,j-1}^n}{2\Delta\eta}P_{ij}\right].
\end{aligned} \tag{A4}$$

This equation is then rearranged to solve for $\omega_{i,j}^{n+1}$ in terms of the vorticity and the velocity fields at time step n. Once the vorticity is progressed in time, the stream function can be solved at time step $n+1$ using spatial central differences [with Eqs. (32)–(36)]:

$$\begin{aligned}&\frac{\Psi_{i+1,j}^{n+1}-2\Psi_{ij}^{n+1}+\Psi_{i-1,j}^{n+1}}{(\Delta\mu)^2}K_{ij}+\frac{\Psi_{i,j+1}^{n+1}-2\Psi_{ij}^{n+1}+\Psi_{i,j-1}^{n+1}}{(\Delta\eta^2)}L_{ij}\\&+2\frac{\Psi_{i+1,j+1}^{n+1}-\Psi_{i+1,j-1}^{n+1}-\Psi_{i-1,j+1}^{n+1}+\Psi_{i-1,j-1}^{n+1}}{4\Delta\mu\Delta\eta}M_{ij}\\&+\frac{\Psi_{i+1,j}^{n+1}-\Psi_{i-1,j}^{n+1}}{2\Delta\mu}N_{ij}+\frac{\Psi_{i,j+1}^{n+1}-\Psi_{i,j-1}^{n+1}}{2\Delta\eta}P_{ij}=-\omega_{i,j}^{n+1}.\end{aligned}\tag{A5}$$

Equation (A5) is solved using a successive over-relaxation iterative technique with an over-relaxation parameter of 1.9 for fastest convergence. A convergence to a given tolerance of 10^{-6} between the maximum difference of ψ, in the whole computational domain, in two successive iterations is used to determine the field of $\Psi_{i,j}^{n+1}$ at time step $n+1$. Then, the velocity field at time step $n+1$ can be determined from

$$\begin{aligned}V_\mu^{n+1}&=\frac{1}{\sqrt{\mu^{2(a-1)}+\eta^2}}\frac{\Psi_{i,j+1}^{n+1}-\Psi_{i,j-1}^{n+1}}{2\Delta\eta},\\V_\eta^{n+1}&=\frac{-1}{\sqrt{\mu^2+\eta^{2(a-1)}}}\frac{\Psi_{i+1,j}^{n+1}-\Psi_{i-1,j}^{n+1}}{2\Delta\mu}.\end{aligned}\tag{A6}$$

The values of V_μ and V_η are computed at the boundaries by a first-order forward or backward difference as needed.

2. Boundary and initial conditions of the inner problem

The equations above are solved under the following boundary conditions: (i) a boundary condition at the wall ($\eta = 1$) given by $\Psi_{1,j=1}^n = 0$ for all $-M \leqslant i \leqslant M$; (ii) an inflow far-field condition, at $\eta = \eta_{\max}$, $\Psi_{i,j=N}^n$, described by the potential flow behavior at the far field; (iii) an outflow condition at $\mu = \pm\mu_{\max}$ given by $\Psi_{i=\pm M,j}^n = \Psi_{i=\pm(M-1),j}^n$ for $1 < j < N$; and (iv) the vorticity, $\omega_{i,j=1}$, is computed for $-M < i < M$ by a second-order forward difference approximation in the j direction that accounts for the wall no-slip condition along a stationary boundary given by $\omega_{i,j=1}^n = (7\psi_{i,j=1}^n - 8\psi_{i,j=2}^n + \psi_{i,j=3}^n)/2(\Delta\eta)^2$.

The computations are initiated for a fixed value of a by establishing the symmetric, viscous flow solution at a given Re_M and $\tilde{A} = 0$. Then, this solution is used as an initial state for the computation of the flow at the same Re_M with an $\tilde{A}$ incrementally increased by small steps of no more than $\tilde{A} = 0.05$. Each time asymptotic state is used as an initial state for computation of the next nearby value of $\tilde{A}$.

3. Numerical stability criteria

The computations must satisfy certain numerical stability criteria. Here, the Courant-Fredrichs-Levy (CFL) number C_k, diffusion number d_k, and the cell Reynolds number Re_C are required to obey certain limitations. These numbers are given by $C_k = U_{\max}\frac{\Delta\tau^*}{\Delta x_k}$, $d_k = \frac{1}{\mathrm{Re}_M}\frac{\Delta\tau^*}{(\Delta x_k)^2}$, and $\mathrm{Re}_C = \Delta x_k \mathrm{Re}_M$. In the present numerical computations, $U_{\max} = 1$ and x_k indicates μ or η. Extending von Neumann numerical linear stability analysis to the current forward-in-time, central-in-space differencing scheme leads to certain stability requirements in a two-dimensional problem given by $C = C_\mu + C_\eta \leqslant 1$, $d = d_\mu + d_\eta \leqslant 1/2$, and $\mathrm{Re}_C \leqslant 4/C$. For sufficiently fine meshes used in the present study ($M = 200$, $N = 200$), the cell Reynolds number criterion is the most restrictive.

Therefore, it is used as the criterion for setting the maximum for $\Delta\tau^*$, thereby dictating small time steps.

Furthermore, Thompson *et al.* [20] state that the cell Reynolds number restriction is too restrictive in determining the size of the time step and therefore larger $\Delta\tau^*$ may be used to achieve stable calculations. Yet, we used it as a buffer against numerical instabilities that may result from nonlinear effects in the flow evolution. Therefore, the CFL number in the present computations is typically less than 0.01, providing high accuracy of resolution of velocity signals in time, particularly for the low-frequency waves shed behind the separation bubble which convect along the nose surface and are involved in the delay of stall.

[1] B. M. Jones, Stalling, J. R. Aeronaut. Soc. **38**, 753 (1934).

[2] E. N. Jacobs and A. Sherman, Airfoil section characteristics as affected by variations of the Reynolds number, National Advisory Council on Aeronautics Tech. Rep. No. 586, 1937.

[3] I. H. Abbott and A. E. von Doenhoff, *Theory of Wing Sections: Including a Summary of Airfoil Data* (Dover, New York, 1959).

[4] I. Tani, Low speed flows involving bubble separations, Progr. Aerospace Sci. **5**, 70 (1964).

[5] M. S. Selig, C. A. Lyon, P. Giguere, C. P. Ninham, and J. J. Guglielmo, *Summary of Low-Speed Airfoil Data* (University of Illinois, Urbana-Champaign, 1996), Vol. 2.

[6] S. C. Yen and L. C. Huang, Flow patterns and aerodynamics performance of unswept and swept-back wings, J. Fluids Engin. **131**, 111101 (2009).

[7] J. Pavelka and K. Tatum, Validation of a wing leading-edge stall prediction technique, J. Aircr. **18**, 849 (1981).

[8] M. J. Werle and R. T. Davis, Incompressible laminar boundary layers on a parabola at angle of attack: A study of the separation point, J. Appl. Mech. **39**, 7 (1972).

[9] K. Stewartson, F. T. Smith, and K. Kaups, Marginal separation, Stud. Appl. Math. **67**, 45 (1982).

[10] A. I. Ruban, Asymptotic theory of short separation regions on the leading edge of a slender airfoil, Fluid Dynamics **17**, 33 (1982).

[11] W. J. Morris and Z. Rusak, Stall onset on airfoils at moderately high Reynolds number flows, J. Fluids Engin. **133**, 111104 (2011).

[12] W. J. Morris and Z. Rusak, Stall onset on aerofoils at low to moderately high Reynolds number flows, J. Fluid Mech. **733**, 439 (2013).

[13] V. V. Sychev, A. I. Ruban, V. V. Sychec, and G. L. Korolev, *Asymptotic Theory of Separated Flows* (Cambridge University Press, Cambridge, UK, 1998).

[14] R. H. Liebeck, A class of airfoils designed for high lift in incompressible flow, J. Aircr. **10**, 610 (1973).

[15] P. Balakumar, Direct numerical simulation of flows over an NACA-0012 airfoil at low and moderate Reynolds numbers, in *47th AIAA Fluid Dynamics Conference, AIAA AVIATION Forum* (AIAA 2017-3978) (2017).

[16] J. D. Cole and L. P. Cook, *Transonic Aerodynamics* (North-Holland, Amsterdam, 1986).

[17] H. Ashley and M. Landahl, *Aerodynamics of Wings and Bodies* (Dover, New York, 1985).

[18] Z. Rusak, Subsonic flow around the leading-edge of a thin aerofoil with a parabolic nose, Eur. J. Appl. Math. **5**, 283 (1994).

[19] B. E. Webster, M. S. Shephard, Z Rusak, and J. E. Flaherty, Automated adaptive time-discontinuous finite element method for unsteady compressible airfoil aerodynamics, AIAA J. **32**, 748 (1994).

[20] H. D. Thompson, B. W. Webb, and J. D. Hoffmann, The cell Reynolds number myth, Int. J. Num. Methods Fluids **5**, 305 (1985).

[21] W. J. Morris, A universal prediction of stall onset for airfoils over a wide range of Reynolds number flow, Ph.D. thesis, Rensselaer Polytechnic Institute, Troy, New York, 2009.

[22] M. Kraljic, The leading-edge stall of airfoils with blunt noses at low to moderately high Reynolds numbers, Ph.D. thesis, Rensselaer Polytechnic Institute, Troy, New York, 2017.

[23] Z. Rusak and J. C. Lee, Transonic small disturbance theory—a tool for aerodynamic analysis and design, Can. Aeron. Space J. **46**, 74 (2000).

[24] D. W. Schwendeman, M. C. A. Kropinski, and J. D. Cole, On the construction and calculation of optimal nonlifting critical airfoils, Z. angew. Math. Phys. **44**, 556 (1993).

[25] Z. Rusak, Transonic flow around the leading edge of a thin airfoil with a parabolic nose, J. Fluid Mech. **248**, 1 (1993).

[26] Z. Rusak, Transonic flow around optimum critical airfoils, SIAM J. Appl. Math. **55**, 1455 (1995).

[27] M. C. A. Kropinski, D. W. Schwendeman, and J. D. Cole, Hodograph design of lifting airfoils with high critical Mach numbers, Theor. Comput. Fluid Dyn. **7**, 173 (1995).

[28] D. P. Raymer, *Aircraft Design: A Conceptual Approach* (American Institute of Aeronautics and Astronautics, Reston, VA, 2012).